Insights into the terminal Ediacaran marine carbonate record from shale-hosted carbonate carbon isotopes

Fred Bowyer[1], Mariana Yilales[1], Rachel Wood[1], and Simon W. Poulton[2]

[1]*School of GeoSciences, University of Edinburgh, James Hutton Road, Edinburgh EH9 3FE, UK.*

[2]*School of Earth and Environment, University of Leeds, Leeds LS2 9JT, UK.*

ABSTRACT. The marine carbon isotope record ($\delta^{13}C$) used for chemostratigraphy and reconstruction of carbon cycle dynamics is commonly assembled using carbonate rocks. There is, however, evidence that carbonate cements hosted within fine-grained clastics (shales and mudstones) in some settings may also express $\delta^{13}C$ trends that covary with the record from carbonates. We present new carbon and oxygen isotopic data from shale-hosted carbonate cements (herein termed $\delta^{13}C_{carb\text{-}sh}$ and $\delta^{18}O_{carb\text{-}sh}$, n = 107, <16 wt% $CaCO_3$) of the terminal Ediacaran Nama Group, Namibia (≥550.5 to <539.6 Million years ago; Ma). These data are compared with the published carbon and oxygen isotopic record from coeval carbonates ($\delta^{13}C_{carb}$ and $\delta^{18}O_{carb}$, n = 1611) and total organic carbon (TOC) concentrations. We show that, in the Nama Group, $\delta^{13}C_{carb\text{-}sh}$ compositions in samples of intermediate to high $CaCO_3$/TOC (>0.4) can approximate contemporaneous $\delta^{13}C_{carb}$ in open marine mixed carbonate-clastic settings. By contrast, $\delta^{13}C_{carb\text{-}sh}$ values in samples with low $CaCO_3$/TOC (<0.4) that were deposited in clastic settings distant from the locus of carbonate deposition are more negative than contemporaneous $\delta^{13}C_{carb}$. These data suggest that $\delta^{13}C_{carb\text{-}sh}$ may approach seawater composition in samples with low TOC when deposited in settings characterized by high CO_3^{2-} concentration, where carbonate can rapidly precipitate from seawater during early diagenesis. However, the use of $\delta^{13}C_{carb\text{-}sh}$ to infill gaps in the existing $\delta^{13}C_{carb}$ record remains uncertain, even when these criteria are fulfilled. Intervals of $\delta^{13}C$-$\delta^{18}O$ co-variability in the Nama Group succession appear to correlate with units where seawater mixing with

meteoric fluids was more likely during early diagenesis, such as clastic-dominated settings, which also show significant decreasing $\delta^{18}O$ through time with gradual sub-basin infill. We further consider uncertainties in lithostratigraphic correlation of the upper Urusis Formation of the Nama Group that enable three new possible correlations to be proposed for $\delta^{13}C_{carb\text{-}sh}$ data within the terminal Ediacaran to lower Cambrian (<542.65 Ma to >535 Ma) regional and global $\delta^{13}C_{carb}$ records.

Keywords: Ediacaran, carbon isotope, chemostratigraphy, organic carbon, diagenesis

1. INTRODUCTION

The marine $\delta^{13}C$ curve is used to understand the evolution of the carbon cycle and for chemostratigraphic correlation through geological time (Cramer & Jarvis, 2020). Long-term changes in seawater $\delta^{13}C$ are often considered to reflect the net production, flux, burial, and oxidation of isotopically light organic matter (e.g., Veizer & Hoefs, 1976). However, local pools of DIC with distinct isotopic composition and sediment-buffered versus fluid-buffered diagenetic regimes may result in significant deviation of the carbon isotopic composition preserved by carbonate cements and sediments ($\delta^{13}C_{carb}$) from global average seawater $\delta^{13}C_{DIC}$ (Ahm & Husson, 2022; Cui et al., 2020; Geyman & Maloof, 2019; Hoffman & Lamothe, 2019; Melim et al., 2002). Notwithstanding these local effects, global composite $\delta^{13}C_{carb}$ records that are calibrated using available radiometric constraints in multiple regions throughout the late Neoproterozoic to early Phanerozoic appear to suggest that numerous $\delta^{13}C_{carb}$ excursions recorded within individual successions may be globally synchronous (e.g., Bowyer et al., 2022; Halverson et al, 2005; Maloof et al., 2010; Yang et al., 2021). These excursions may therefore be driven by globally synchronous processes including, but not limited to, changes in the relative volumes of siliciclastic vs carbonate sedimentation, nutrient delivery, or eustatic sea level (Ahm et al., 2021).

The $\delta^{13}C$ record is assembled using carbonate rocks or bioclasts, but clastic rocks (sandstones, siltstones, shales or conglomerates) are commonly excluded because their authigenic carbonate cements are assumed to have precipitated later under burial diagenetic conditions, rather than from seawater. However, carbonate cements within some Neoproterozoic clastic rocks have also recently been shown to record trends in $\delta^{13}C$ that are radiometrically calibrated to be synchronous with global excursions in the $\delta^{13}C$ record derived from coeval carbonate rocks, albeit with some variable offsets (Canfield et al., 2020). This raises the possibility that $\delta^{13}C$ data derived from shale-hosted carbonate cements (herein termed $\delta^{13}C_{carb-sh}$ to aid distinction from $\delta^{13}C_{carb}$ of coeval carbonates), in some depositional and diagenetic settings, may be useful to establish stratigraphic correlations and to infer carbon cycle behaviour in otherwise poorly constrained clastic successions. A crucial pre-requisite for the application of $\delta^{13}C_{carb-sh}$ for chemostratigraphy is to understand the mechanisms for, and extent of, $\delta^{13}C_{carb-sh}$ deviation from regional $\delta^{13}C_{carb}$ records.

The isotopic composition of a carbonate mineral is dependent upon the composition of the solution from which it precipitates, and the effects of post-depositional diagenetic alteration (e.g., Ahm et al., 2018; Swart, 2015). The oxygen isotopic composition ($\delta^{18}O$) of inorganic carbonates is largely dependent upon the $\delta^{18}O$ composition of the precipitating fluid, the temperature of precipitation, and the resulting carbonate mineralogy (e.g., Epstein et al., 1953; Epstein & Mayeda, 1953; Tarutani et al., 1969; Urey, 1947). Seawater is generally enriched in ^{18}O relative to freshwater, and carbonate precipitates that are altered within the meteoric mixing zone therefore commonly show positive covariation between $\delta^{13}C$ and $\delta^{18}O$ that reflects these two end-member solution compositions (Allan & Matthews, 1982; Swart, 2015). Lower values of $\delta^{18}O$ are also associated with higher burial temperatures (Urey, 1947), and co-variation between $\delta^{13}C$ and $\delta^{18}O$ may therefore also occur as a consequence of mixing between low temperature, fluid-buffered carbonates and high temperature, sediment-buffered carbonates (Ahm et al., 2018).

Here we present new $\delta^{13}C_{carb-sh}$ data from the fossiliferous terminal Ediacaran Nama Group, Namibia (≥550.5 Ma to <539.6 Ma). The succession comprises mixed carbonates and clastics with well-established intra- and inter-basinal correlations and abundant dated ash beds, but the regional composite $\delta^{13}C_{carb}$ curve is discontinuous (Bowyer et al., 2022; Germs, 1983; Germs & Gresse, 1991; Linnemann et al., 2019; Nelson et al., 2022; Saylor et al., 1998; Wood et al., 2015). A proposed chemostratigraphic marker for the Ediacaran-Cambrian boundary corresponds to the stratigraphic position of a large magnitude negative $\delta^{13}C_{carb}$ excursion, termed the '1n/BACE' (min. $\delta^{13}C_{carb}$ = ~-10‰), relative to key fossil occurrences, including the first appearance datum (FAD) of the ichnospecies *Treptichnus pedum* (Brasier et al., 1994; Zhu et al., 2006). Numerous uncertainties remain, however, in the precise ages of the 1n/BACE onset and recovery (reviewed in Bowyer et al., 2022), and the sequence of regional and global biotic first appearances across the 1n/BACE (e.g., Bowyer et al., 2023; Topper et al., 2022). The 1n/BACE has been recorded in multiple successions globally (e.g., Hodgin et al., 2020; Kouchinsky et al., 2007; Maloof et al., 2010; Smith et al., 2016; Topper et al., 2022; Zhu et al., 2019), but is notably absent from the Nama Group (Nelson et al., 2022; Saylor et al., 1998; Wood et al., 2015). This may suggest that the onset of this excursion is younger than ca. 538 Ma, and therefore postdates carbonate sedimentation in the Nama Group succession (Bowyer et al., 2022, 2023; Nelson et al., 2022).

We assess the potential for siliciclastic rocks to record $\delta^{13}C$ values that approximate seawater composition throughout deposition of the Nama Group. First, measurements of $\delta^{13}C_{carb\text{-}sh}$ are compared with the magnitudes and trends in $\delta^{13}C_{carb}$ recorded by carbonate interbeds and laterally correlative carbonate-clastic successions. We then interrogate stratigraphic intervals that show covariation between $\delta^{13}C$ and $\delta^{18}O$, using published carbonate data and new clastic data, to identify possible alteration of $\delta^{13}C$ from seawater composition associated with meteoric diagenesis. Covariation between $\delta^{13}C_{carb\text{-}sh}$ and the concentrations of calcium carbonate ($CaCO_3$) and total organic carbon (TOC) are also evaluated in order to explore the potential for differences in bulk shale composition to result in deviation of $\delta^{13}C_{carb\text{-}sh}$ from $\delta^{13}C_{carb}$. Lastly, we explore the chemostratigraphic alignment of new $\delta^{13}C_{carb\text{-}sh}$ data within alternative lithostratigraphic correlations for the Urusis Formation of the Nama Group (≤543 to ≤538.6 Ma), and consider the utility of the $\delta^{13}C_{carb\text{-}sh}$ data to infill gaps in the composite regional $\delta^{13}C$ curve across the critical ≥550.5 to <538 Ma interval. We compare the composite $\delta^{13}C$ record for the upper Nama Group with regional composite $\delta^{13}C$ records from other approximately-contemporaneous successions deposited across the terminal Ediacaran to lowermost Cambrian interval, in order to evaluate the inter-regional consistency of magnitudes and trends in $\delta^{13}C$ and the implications for calibrated global biostratigraphy.

2. GEOLOGICAL SETTING OF THE NAMA GROUP

The Nama Group in southern Namibia (≥550.5 to <538 Ma) is a mixed carbonate and siliciclastic foreland basin succession deposited in supratidal to outer ramp settings in the Zaris and Witputs sub-basins (fig. 1A; Germs, 1983; Gresse & Germs, 1993). Sediments within the Zaris and Witputs sub-basins were deposited during cratonic convergence along the Damara and Gariep orogenies, to the north and southwest, respectively (Germs, 1983; Germs & Gresse, 1991; Gresse & Germs, 1993). Strata within both sub-basins have been correlated using litho- and chemostratigraphy, and correlation of stratal stacking patterns have informed sequence stratigraphy (figs. 1 and 2; e.g., Germs, 1983; Saylor et al., 1995, 1998; Wood et al., 2015). Intervals of the Nama Group succession have also been accurately age-calibrated via U-Pb zircon geochronology of interbedded tuff deposits (fig. 2; Bowring et al., 2007; Grotzinger et al., 1995; Linnemann et al., 2019; Nelson et al., 2022). The age of the base of the Nama Group remains uncertain, but is estimated to be ≥550.5 Ma (Bowyer et al., 2022; Saylor et al., 1998), and the youngest dated tuff deposit in the Witputs Sub-basin, immediately overlying the sub-Nomtsas Formation unconformity, yields a U-Pb age of 538.58 ± 0.19 Ma (Linnemann et al., 2019).

The succession is divided into the lower Nama Group (Kuibis Subgroup, ca. ≥550.5 to <547 Ma), and upper Nama Group (Schwarzrand Subgroup, ca. ≥546 to <538 Ma; fig. 1). A mixed carbonate-siliciclastic succession deposited in the Vioolsdrif Sub-basin of northwest South Africa is radiometrically constrained to be temporally equivalent to, at minimum, the Schwarzrand Subgroup of the Witputs Sub-basin (Nelson et al., 2022). The Witputs and Vioolsdrif sub-basins may have been separated by a tectonic forebulge (the Koedoelaagte Arch; Germs & Gresse, 1991).

The Zaris and Witputs sub-basins deepened to the (present-day) north and southwest, respectively, during deposition of the Kuibis Subgroup, with increasing distance from an intervening paleobathymetric high (the Osis Arch), and with distance from the Kalahari Craton to the present east (fig. 1B; Germs, 1983). However, gradual infill of the Zaris Sub-basin shifted the orientation of facies belts to northwest-southeast across both sub-basins during deposition of the Schwarzrand Subgroup (fig. 1C; Germs, 1983; Saylor et al., 1995; Saylor, 2003). Facies belts range from clastic-dominated braided-fluvial to muddy tidal, to inner, mid- and finally outer ramp carbonate-dominated facies, which deepened, on average, to the west or south-west during deposition of the Schwarzrand Subgroup (Germs, 1983; Saylor, 2003). The Kalahari craton was the main source of clastic sediment into the Nama sub-basins during deposition of the Kuibis Subgroup (fig. 1B; Germs, 1983), but during deposition of the Schwarzrand Subgroup, the Zaris Sub-basin received additional detrital material directly from the Damara Belt to the north (fig. 1C; Blanco et al., 2009, 2011; Germs, 1983). In the Nama Group successions, early Transgressive Systems Tracts are generally dominated by siliciclastic rocks whereas various carbonate facies distinguish late Transgressive to Highstand Systems Tracts (Saylor et al., 1995, 1998).

3. METHODS

$\delta^{13}C_{carb\text{-}sh}$ and $\delta^{18}O_{carb\text{-}sh}$ data were obtained from 107 shale/mudstone samples (defined as <16 wt% $CaCO_3$) collected from eight outcrop sections distributed across both the Zaris and Witputs sub-basins, which together cover ≥12 Myr from the Kanies Member of the Dabis Formation (≥550.5 Ma) to the Nomtsas Formation (≤538.6 Ma; fig. 2, table A1). Samples were taken from three settings: (1) three sections of the lower Kuibis Subgroup that contain intervals composed of decimeter to meter-scale interbedded carbonates and clastics (≤1 m) deposited on the inner to mid-outer ramp (n = 21, sections 6, 9 and 10; figs. 1B, 2, 3A,B); (2) three extended shale packages (12–90 m) within carbonate-clastic successions, one from a shallow-inner ramp section of the Kuibis Subgroup (n = 3, section 8; figs. 1B and 2), and two from the Schwarzrand Subgroup deposited on the mid- to outer ramp (n = 21, sections 3 and 4; figs. 1C, 2, 3C–E); (3) two composite sampling transects through clastic-only successions of the uppermost Kuibis Subgroup and entire Schwarzrand Subgroup (n = 62, sections 11 and 12; figs. 1B and C, 2, 3F,G) that record an overall shallowing-upward succession from mid-ramp to inner ramp and lagoon. Samples from these three settings are classified into three groups: Group 1: m-scale shale interbeds within carbonate-clastic successions; Group 2: extended shale packages within carbonate-clastic successions, and Group 3: clastic-only successions.

Analyses of $\delta^{13}C_{carb-sh}$ followed the method of Canfield et al. (2020). Powdered bulk clastic rock samples in sealed vials were reacted with 100% orthophosphoric acid at 75°C and left for 24 h using an Elementar iso FLOW system. Any resulting CO_2 gas produced was then extracted from the vial and analyzed for its carbon and oxygen isotopic ratios using an Elementar PRECISION stable isotope ratio mass spectrometer. The standard deviation (n = 48) of a powdered coral laboratory standard (COR1D, $\delta^{13}C$ = -0.649‰, $\delta^{18}O$ = -4.924‰) run as a sample on the same days as the study samples, was ± 0.074‰ for $\delta^{13}C_{carb}$ and ± 0.111‰ for $\delta^{18}O_{carb}$. All isotopic values are normalized relative to the Vienna Pee Dee Belemnite (VPDB) standard. Total wt% $CaCO_3$ in shales was estimated using a linear regression model between peak height area from the isotopic measurements and the analysed mass of powdered coral laboratory standard (COR1D, assumed 100% $CaCO_3$). The uncertainty associated with this regression model is <1% (see Appendix). A subset of shale samples of varying $CaCO_3$ concentration from different sections were also analysed by colorimeter, and the relative concentrations of $CaCO_3$ were consistent between both methods (table A2). We also consider published TOC concentration data from the same samples analysed herein for $\delta^{13}C_{carb-sh}$ (Bowyer et al., 2020).

$\delta^{13}C_{carb-sh}$ data (n = 107) were compared to available $\delta^{13}C_{carb}$ from 38 sections (n = 1611) of the Nama Group succession in Namibia and northwest South Africa. In order to test the degree to which these data may reflect early diagenetic resetting from seawater $\delta^{13}C$ composition associated with mixing between two end-member compositions, we assessed the co-variation of $\delta^{13}C$ and $\delta^{18}O$. In order to test whether values of $\delta^{13}C_{carb-sh}$ are affected by the concentrations of $CaCO_3$ or TOC within each sample, we tested the co-variation of $\delta^{13}C_{carb-sh}$ and $CaCO_3$, and $\delta^{13}C_{carb-sh}$ and TOC. In each case, the Shapiro-Wilk test was used to evaluate whether these data are normally distributed (tables A3 and A4). The strength and significance of correlations were tested using either Pearson's correlation coefficient (r), or the non-parametric equivalent test of Spearman's rank correlation coefficient (ρ). Spearman's rank correlation coefficient was used when assumptions about the normality of the distribution of the variables, constant residual variability, and linearity were not fulfilled. In each case, significant correlations are indicated when $p \leq 0.05$.

Lastly, we explore the alternative regional $\delta^{13}C$ chemostratigraphies that result from different possible lithostratigraphic correlations between sections of the Urusis Formation within the Witputs Sub-basin and between the Witputs and Vioolsdrif sub-basins. All new and existing data are calibrated with available radiometric dates, and placed within the resulting composite Nama Group $\delta^{13}C$ chemostratigraphic age frameworks (updated from Bowyer et al., 2022, 2023).

4. RESULTS

4.1. Group 1: Meter-scale shale interbeds within carbonate-clastic successions

The $\delta^{13}C_{carb\text{-}sh}$ data for m-scale shale interbeds within carbonate-clastic successions range from -6.63‰ to +2.50‰ (mean = -1.62‰, sd = 2.38‰, n = 21, table A1). Through the Dabis Formation and lower Zaris Formation (≥550.5 to ca. 547 Ma), $\delta^{13}C_{carb\text{-}sh}$ values from Arasab, Omkyk and Brak (sections 6, 9, 10, fig. 2) closely follow the negative-to-positive trend recorded by contemporaneous $\delta^{13}C_{carb}$ (fig. 2).

$\delta^{13}C_{carb\text{-}sh}$ values do not show a statistically significant correlation with $\delta^{18}O_{carb\text{-}sh}$ ($r = 0.42$, $p = 0.06$, $R^2 = 0.17$, fig. 4A). These interbedded shales are characterized by $CaCO_3$ concentrations in the range 0.02–15.51 wt% (mean = 2.42 wt%, fig. 4B), TOC concentrations in the range 0.04–0.11 wt% (mean = 0.07 wt%, fig. 4C), and $CaCO_3$/TOC in the range 0.4–85.0 (mean = 11.83, fig. 4D). There is no significant correlation between $\delta^{13}C_{carb\text{-}sh}$ and $CaCO_3$ content ($\rho = 0.07$, $p = 0.77$, fig. 4B), $\delta^{13}C_{carb\text{-}sh}$ and TOC content ($\rho = -0.49$, $p = 0.15$, fig. 4C), or $\delta^{13}C_{carb\text{-}sh}$ and $CaCO_3$/TOC ($\rho = -0.32$, $p = 0.37$, fig. 4D).

4.2. Group 2: Extended shale packages within carbonate-clastic successions

Values of $\delta^{13}C_{carb\text{-}sh}$ from a 12.5 m-thick shale package of the Dabis Formation (Kuibis Subgroup, ca. 550.5 Ma) at Zwartmodder (section 8, fig. 2) range from -7.18‰ to -2.38‰ (n = 3). This interval records siliciclastic deposition during initial transgression across the Kalahari basement, and has been litho- and chemostratigraphically correlated with transgressive limestone, dolostone and shale of the basal Omkyk Member at Omkyk (section 9), and the dolostone-dominated Dabis Formation at Brak (sections 10, fig. 2;

Wood et al., 2015). $\delta^{13}C_{carb-sh}$ data at Zwartmodder overlap in magnitude and trend with both $\delta^{13}C_{carb-sh}$ and $\delta^{13}C_{carb}$ at Omkyk and Brak throughout this interval (figs. 2 and 4E).

$\delta^{13}C_{carb-sh}$ data from extended shale packages of the Urusis Formation (≤543 to ≤538.6 Ma), comprising the Swartpunt (section 3) and Swartkloofberg (section 4) sections, show dominantly negative values that range from -8.52‰ to +0.17‰ (mean = -4.01‰, sd = 2.69, n = 21, figs. 2 and 4E). $\delta^{13}C_{carb-sh}$ values at section 3 (-8.52‰ to +0.17‰, mean = -3.16‰, sd = 2.24, n = 12) appear scattered and depleted relative to $\delta^{13}C_{carb}$ above and below the siliciclastic interval (0.33–1.84‰, mean = 1.32‰, n = 36). However, $\delta^{13}C_{carb-sh}$ values at section 4 (-8.12‰ to -0.40‰, mean = -5.14‰, sd = 2.95, n = 9) broadly display both a falling limb from $\delta^{13}C_{carb}$ values recorded by underlying pinnacle reef carbonate (0.63–1.72‰, mean = 1.24, n = 4), followed by a nadir and a rising limb, which together appear to track the overall shape of a negative $\delta^{13}C_{carb-sh}$ excursion (fig. 2).

Group 2 shales do not show a statistically significant correlation between $\delta^{13}C_{carb-sh}$ and $\delta^{18}O_{carb-sh}$ ($r = 0.37$, $p = 0.08$, $R^2 = 0.13$; fig. 4E). These shale packages have $CaCO_3$ concentrations in the range 0.01–4.43 wt% (mean = 1.05 wt%, fig. 4F), TOC concentrations in the range 0.05–0.19 wt% (mean = 0.08 wt%, fig. 4G), and $CaCO_3$/TOC in the range 0.1–54.8 (mean = 18.49, fig. 4H). There is no statistically significant correlation between $\delta^{13}C_{carb-sh}$ and $CaCO_3$ content ($\rho = 0.31$, $p = 0.14$, fig. 4F), $\delta^{13}C_{carb-sh}$ and TOC content ($\rho = -0.34$, $p = 0.28$, fig. 4G), or $\delta^{13}C_{carb-sh}$ and $CaCO_3$/TOC ($r = 0.23$, $p = 0.47$, $R^2 = 0.05$, fig. 4H).

4.3. Group 3: Clastic-only successions

$\delta^{13}C_{carb-sh}$ data from one clastic-only succession of the Urikos Member and Nudaus Formation of the Zaris Sub-basin (section 11, fig. 2), and a second composite clastic-only succession of the Urikos Member, and Nudaus, Urusis and Nomtsas formations of the Zaris Sub-basin (section 12, fig. 2), range from -15.45‰ to -1.00‰ (mean = -7.72‰, sd = 3.31, n = 62). These data are significantly depleted relative to $\delta^{13}C$ values of contemporaneous carbonates and shales from carbonate-clastic successions of the Zaris and Witputs sub-basins (figs. 2, 4I), and show a strong and statistically significant positive correlation between $\delta^{13}C_{carb-sh}$ and $\delta^{18}O_{carb-sh}$ ($\rho = 0.70$, $p < 0.01$, fig. 4I). This positive correlation also appears to be associated with the temporal distribution of samples, whereby values of $\delta^{13}C_{carb-sh}$ and $\delta^{18}O_{carb-sh}$ increase with relative age (figs. 2 and 4I).

With the exception of some of the oldest samples, the $CaCO_3$ content of Group 3 shales is lower than shales from groups 1 and 2, ranging from 0.00–3.16 wt% (mean = 0.09 wt%, fig. 4J). Group 3 shales have TOC concentrations in the range 0.05–0.10 wt% (mean = 0.08 wt%, fig. 4K) and $CaCO_3$/TOC in the range 0.1–0.4 (mean = 0.11, fig. 4L). There is a significant positive correlation between $\delta^{13}C_{carb-sh}$ and $CaCO_3$ content (ρ = 0.57, $p < 0.01$, fig. 4J), but no significant correlation observed between $\delta^{13}C_{carb-sh}$ and TOC content ($r = 0.56$, $p = 0.09$, $R^2 = 0.31$ fig. 4K), or $\delta^{13}C_{carb-sh}$ and $CaCO_3$/TOC (ρ = -0.43, $p = 0.29$, fig. 4L).

4.4. Qualitative observations of $\delta^{13}C$ and $\delta^{18}O$ through the Nama Group

Carbonates that were deposited following initial transgressive onlap of the Nama basement record negative values of $\delta^{13}C_{carb}$ that correspond to the 'basal Nama excursion' (BANE; Bowyer et al., 2022; Maloney et al., 2020; Saylor et al., 1998; Smith, 1999; Wood et al., 2015). Following the BANE, $\delta^{13}C_{carb}$ values increase through the lower Omkyk Member (Zaris Sub-basin) and Kliphoek and Mooifontein members (Witputs Sub-basin), to reach peak values (~5‰) associated with the Omkyk excursion (OME, fig. 2; Bowyer et al., 2022; Saylor et al., 1998; Smith, 1999; Wood et al., 2015). Following the OME interval, $\delta^{13}C_{carb}$ values show a gradual decrease towards a minor negative excursion (Saylor et al., 1998). This interval has been tentatively correlated with a negative $\delta^{13}C_{carb}$ excursion recorded in the A0 Member of the Ara Group, Oman, based on a preliminary global chemostratigraphic correlation anchored by available radiometric data from tuff interbeds in the underlying Hoogland Member of the Nama Group and A0 Member of the Ara Group (Bowring et al., 2007). This negative excursion has therefore been termed the 'A0' excursion, for ease of reference (but see discussion of uncertainty in Bowyer et al., 2022).

In the Schwarzrand Subgroup of the Witputs Sub-basin, carbonates of the lower Huns Member record recovery from a positive $\delta^{13}C_{carb}$ excursion (max $\delta^{13}C_{carb}$ = 4.24‰, section 1, fig. 2). This interval stratigraphically overlies the Nasep Member, wherein a tuff bed at a neighbouring section to the north of section 1 has been dated to 542.65 ±

0.15 Ma (Nelson et al., 2022). The $\delta^{13}C_{carb}$ peak recorded in the lower Huns Member at section 1 has been tentatively correlated with radiometrically-constrained positive $\delta^{13}C_{carb}$ values in the Tamengo Formation of Brazil (Boggiani et al., 2010; Parry et al., 2017) and the A3 Member of the Ara Group, Oman (Bowring et al., 2007). This interval of positive $\delta^{13}C_{carb}$ has therefore been termed the 'A3' excursion (Bowyer et al., 2022).

A compilation of all Nama Group carbonate data shows no correlation between $\delta^{13}C_{carb}$ and $\delta^{18}O_{carb}$ ($\rho = -0.09$, $p < 0.01$, fig. 4M). However, individual sections and discrete intervals of the Nama Group record are characterized by significant correlation between $\delta^{13}C_{carb}$ and $\delta^{18}O_{carb}$ (fig. 2). As such, we consider associated temporal changes in $\delta^{13}C$ and $\delta^{18}O$, and differences in recorded values between carbonates and shales, through the Nama Group succession.

In the Kuibis Subgroup, Group 1 and Group 2 shales show generally reciprocal trends in $\delta^{13}C$ and $\delta^{18}O$ relative to carbonates within individual sections, and between contemporaneous sections, recording the BANE (fig. 2). Carbonates in the lowermost 10–20 m of this interval at sections 5, 8, 9 and 10, record increasing $\delta^{18}O_{carb}$ values that broadly covary with $\delta^{13}C_{carb}$ (fig. 2). Throughout this interval, $\delta^{13}C_{carb\text{-}sh}$ values of Group 1 shales at sections 9 and 10 and Group 2 shales at section 8, and $\delta^{18}O_{carb\text{-}sh}$ values of Group 1 shales at section 10 and Group 2 shales at section 8, covary in magnitude and trend with $\delta^{13}C_{carb}$ and $\delta^{18}O_{carb}$, respectively. Group 1 shales in the lowermost 10 m of section 9 record values of $\delta^{18}O_{carb\text{-}sh}$ that are more positive than interbedded $\delta^{18}O_{carb}$ (fig. 2). By contrast, in the Mara Member of the Witputs Sub-basin, carbonates at sections 6 and 7, and Group 1 shales at section 6, record scattered negative $\delta^{13}C$ values that correspond to the BANE, but show no positive correlation between $\delta^{13}C$ and $\delta^{18}O$ (fig. 2). Indeed, trends in $\delta^{13}C_{carb}$ and $\delta^{18}O_{carb}$ appear to be negatively correlated throughout this interval at section 7 (fig. 2).

Throughout the OME interval, there is no significant correlation between $\delta^{13}C_{carb}$ and $\delta^{18}O_{carb}$ in any section. Following the OME, $\delta^{13}C_{carb}$ values show a gradual decrease towards a minor negative excursion in the Urikos Member (or upper Hoogland Member) at one section to the northwest of section 9 (Zebra River, not shown on fig. 2), which is associated with positive correlation between $\delta^{13}C_{carb}$ and $\delta^{18}O_{carb}$ (Saylor et al., 1998).

Following the A3 excursion, carbonates of the Urusis Formation in the Witputs Sub-basin (sections 1–4, fig. 2) show limited variability in $\delta^{13}C_{carb}$ (-0.80‰ to 2.40‰, mean = 1.34‰, sd = 0.48) and no observable correlation between $\delta^{13}C_{carb}$ and $\delta^{18}O_{carb}$ (fig. 2). Values of $\delta^{18}O_{carb-sh}$ in Group 2 shales at sections 3 and 4 (-9.96‰ to -3.08‰, mean = -6.93‰, sd = 1.84) overlap with, or are more positive than, $\delta^{18}O_{carb}$ of approximately contemporaneous carbonates throughout this interval of the Neint Nababeep Plateau composite section (-9.39‰ to -4.87‰, mean = -6.99‰, sd = 1.15, figs. 2 and 4E).

In the Schwarzrand Subgroup of the Zaris Sub-basin, Group 3 shales at sections 11 and 12 are characterized by decreasing $\delta^{13}C_{carb-sh}$ and $\delta^{18}O_{carb-sh}$ up through the stratigraphic succession (fig. 2), and corresponding positive covariation between $\delta^{13}C_{carb-sh}$ and $\delta^{18}O_{carb-sh}$ (fig. 4I). These values are significantly depleted relative to $\delta^{13}C_{carb}$ and $\delta^{18}O_{carb}$ in samples of the contemporaneous mixed carbonate-clastic succession of the Witputs Sub-basin (sections 1–4, figs. 2, 4I).

5. DISCUSSION

5.1. $\delta^{13}C$ and $\delta^{18}O$ covariation and potential meteoric influence

Sedimentary rocks of the lower Kuibis Subgroup record diachronous deposition across basement rocks of the Kalahari craton in both the Zaris and Witputs sub-basins (Germs, 1974, 1983). As such, the thickest measured sections of the lower Nama Group that accumulated in the deeper parts of each sub-basin (e.g., sections 7 and 10) where accommodation space was greatest, also contain the oldest units. This is supported not only by lithostratigraphic and sequence stratigraphic correlation, but also by observations of $\delta^{13}C_{carb}$ chemostratigraphy and associated preliminary biostratigraphic considerations in both sub-basins (fig. 2; Maloney et al., 2020; Saylor et al., 1995, 1998; Smith, 1999; Wood et al., 2015).

The oldest transgressive carbonates and shale-hosted carbonate cements at all studied sections record recovery from a negative $\delta^{13}C$ excursion (fig. 2). This interval is also characterized by a general shift in dominant lithology from dolostone to limestone, where the $\delta^{13}C$ trend is recorded in both dolostones and limestones within and between individual sections. In the lowermost 10–20 m of sections 5, 8, 9 and 10, this $\delta^{13}C_{carb}$ recovery is accompanied by significant $\delta^{13}C_{carb}$-$\delta^{18}O_{carb}$ covariation, with a corresponding increase in $\delta^{18}O_{carb}$ (fig. 2). By contrast, basal transgressive deposits of the Dabis Formation in the Witputs Sub-basin at sections 6 and 7 do not show any clear positive correlation between $\delta^{13}C_{carb}$ and $\delta^{18}O_{carb}$ (fig. 2). Carbonates of the Mara Member in section 6 are frequently characterized by evaporitic fabrics, and show scattered values of $\delta^{13}C_{carb}$ and $\delta^{18}O_{carb}$, whilst carbonates at section 7 show a general negative correlation between $\delta^{13}C_{carb}$ and $\delta^{18}O_{carb}$ through the lower ~50–75 m (fig. 2; Wood et al., 2015).

Carbonates of the lower Nama Group were deposited upon granitic basement rock, where the $\delta^{13}C$ of freshwater input was likely depleted due to the dominant influence of organic carbon respiration and lack of carbonate weathering that would otherwise contribute elevated $\delta^{13}C_{carb}$ (Khadka et al., 2014; Rodriguez Blanco et al., 2020). Positive $\delta^{13}C_{carb}$-$\delta^{18}O_{carb}$ covariation and low initial $\delta^{13}C_{carb}$ recorded in the lowermost 10–20 m of transgressive carbonate deposits in sections 5, 8, 9 and 10 may therefore reflect a greater degree of mixing between marine and freshwater associated with meteoric diagenesis. However, the overall trend from negative to positive $\delta^{13}C_{carb}$ recorded across the boundary between the Kanies and lower Omkyk members at section 10, and within the Kliphoek Member at sections 6 and 7, is accompanied by no synchronous positive shift in $\delta^{18}O_{carb}$ (fig. 2). Therefore, the degree to which meteoric diagenesis has altered $\delta^{13}C_{carb}$ from the composition of seawater DIC remains uncertain.

The recovery from a negative $\delta^{13}C_{carb}$ excursion recorded by dolomite of the Dengying Formation, South China, is radiometrically constrained to be <550.14 ± 0.63 Ma (Yang et al., 2021), and may correlate with the trend in $\delta^{13}C_{carb}$ recorded by carbonates of the lower Nama Group (Bowring et al., 2007; Saylor et al., 1998; Yang et al., 2021). However, $\delta^{13}C_{carb}$ values of the basal Nama Group are notably depleted relative to all other global $\delta^{13}C_{carb}$ data that postdate the Shuram $\delta^{13}C_{carb}$ excursion (ca. 575−565 Ma; Rooney et al., 2020; Yang et al., 2021) but pre-date the 1n/BACE. Therefore, if the BANE is distinct from the Shuram excursion, as suggested by current global chemostratigraphic age models (Bowyer et al., 2022; Rooney et al., 2020; Yang et al., 2021), then the magnitude of the BANE may reflect regional amplification of negative $\delta^{13}C_{carb}$ values associated with local meteoric diagenesis.

Positive correlation between $\delta^{13}C_{carb}$ and $\delta^{18}O_{carb}$ is also recorded in carbonate interbeds of the Urikos Member (or upper Hoogland Member) of the Zebra River section (to the northwest of section 9), coincident with the inferred A0 negative $\delta^{13}C_{carb}$ excursion (Bowyer et al., 2022; Saylor et al., 1998). Lateral differences in $\delta^{13}C_{carb}$ recorded between sections in the vicinity of Zebra River, and meteoric dissolution of ooids observed within the upper Hoogland Member, have previously been suggested as possible evidence to support deviation of $\delta^{13}C_{carb}$ from the composition of seawater $\delta^{13}C_{DIC}$ in this interval associated with diagenetic alteration (Smith, 1999). Alternatively, the observed differences in trend and magnitude of $\delta^{13}C_{carb}$ between these sections may record lateral differences in section completeness associated with increasing paleodepth and accommodation space from southeast to northwest within the Zaris Sub-basin.

Group 3 shale samples in sections 11 and 12 also show positive covariation between $\delta^{13}C_{carb\text{-}sh}$ and $\delta^{18}O_{carb\text{-}sh}$, and decreasing values of both $\delta^{13}C_{carb\text{-}sh}$ and $\delta^{18}O_{carb\text{-}sh}$ during progressive infill and shallowing of the Zaris Sub-basin (figs. 2 and 4I). At this time, paleocurrent data indicate that clastic input to the Zaris Sub-basin was sourced from the present north and east (fig. 1C; Germs, 1983). Group 3 shales were deposited distant from the locus of carbonate sedimentation (Saylor et al., 1995; Germs, 1983; Gresse & Germs, 1993). Due to outcrop availability, samples were taken along road transects, and record increasing proximity to the source of clastic input with decreasing age (fig. 1C). As such, an increase in the contribution of isotopically light riverine freshwater to $\delta^{13}C_{carb\text{-}sh}$ with decreasing age appears to be the most parsimonious explanation for the significant deviation of $\delta^{13}C_{carb\text{-}sh}$ in Group 3 samples, relative to contemporaneous $\delta^{13}C_{carb}$ recorded throughout the carbonate-clastic succession of the Schwarzrand Subgroup in the Witputs Sub-basin (figs. 2, 4I).

5.2. Potential significance of $\delta^{13}C_{carb\text{-}sh}$ data from carbonate-clastic successions

The isotopic composition of marine carbonates is commonly considered to approximate the isotopic composition of DIC in seawater, provided that precipitated carbonate minerals have not undergone significant subsequent diagenetic alteration. In the Kuibis Subgroup, whole rock carbonates and carbonate cements within Group 1 and Group 2 shales show $\delta^{13}C$ values that are consistent in magnitude and trend (fig. 2). We may infer this to reflect a consistent source for the measured carbonate, potentially seawater DIC.

Nama Group reef carbonates from the Omkyk Member show multiple phases of syndepositional through to late burial cements (Wood et al., 2018), but the timing and type of carbonate cements found in Nama Group clastics is not known, and indeed these may potentially have formed at any time during diagenesis, and from any diagenetic fluid. $\delta^{13}C$ and $\delta^{18}O$ values will only show a correlation in scenarios where there is mixing between different end-members of alteration or by mixing of two different diagenetic fluids. For example, in meteorically-altered carbonates the most altered end-member will have low $\delta^{13}C$ and $\delta^{18}O$, while the least altered end-member will show high $\delta^{13}C$ and $\delta^{18}O$ values relative to contemporaneous seawater DIC, and a similar trend can also be created by mixing of two different diagenetic fluids such as seawater and meteoric water. Values of $\delta^{13}C_{carb-sh}$ from Group 1 and 2 shales in carbonate-clastic successions show no significant correlation with $\delta^{18}O_{carb-sh}$, which may suggest that they formed from a single diagenetic fluid and during a single diagenetic stage (fig. 4A, E). By contrast, Group 3 shales in clastic-only successions show a statistically significant positive correlation between $\delta^{13}C_{carb-sh}$ and $\delta^{18}O_{carb-sh}$, and more negative and variable $\delta^{13}C_{carb-sh}$ values than contemporaneous $\delta^{13}C_{carb}$ (fig. 4I), and so may therefore have formed by either a mixture of variably diagenetically-altered end-members, or via the mixing of two different diagenetic fluids.

5.3. $\delta^{13}C_{carb-sh}$, organic carbon and $CaCO_3$ content

Bulk $\delta^{13}C$ values derived from impure carbonates can deviate from the composition of seawater DIC due to the incorporation of organic matter and subsequent formation of authigenic carbonate during diagenesis. This deviation is most likely to occur in sediments with low carbonate content relative to organic carbon (Saltzman & Thomas, 2012). Scattered negative $\delta^{13}C_{carb}$ values recorded from samples of the Neint Nababeep Plateau composite section have also been associated with stratigraphic proximity to siliciclastic-rich intervals, and have thus not been considered useful for basin-wide $\delta^{13}C$ correlation (Nelson et al., 2022).

Group 1 and 2 shales were deposited in settings where CO_3^{2-} concentrations are inferred to have been high, consistent with contemporaneous, laterally extensive carbonate platform development. In such settings, authigenic carbonate may readily precipitate from seawater. Clastic-hosted carbonate cements from samples of the mixed carbonate-clastic Isaac Formation of the Ediacaran Windermere Supergroup of Laurentia have similarly been shown to record $\delta^{13}C$ values that approximate contemporaneous $\delta^{13}C_{carb}$ (Canfield et al., 2020; Cochrane et al., 2019). We infer that seawater was the primary DIC source for precipitation of carbonate cements in Group 1 shales given elevated concentrations of $CaCO_3$ (0.02–11.96 wt%, mean = 1.77 wt%) compared to Group 3 shales from clastic-only successions (0.00–3.16 wt%, mean = 0.22 wt%), and the consistency between $\delta^{13}C_{carb\text{-}sh}$ in Group 1 shales and $\delta^{13}C_{carb}$ from associated, interbedded carbonates (figs. 2 and 4A). Group 2 shales have an intermediate range of $CaCO_3$ concentrations (0.00–4.43 wt%) relative to shales from groups 1 and 3, and a mean $CaCO_3$ concentration (1.05 wt%) that is elevated relative to Group 3 shales. The median $CaCO_3$ concentration of Group 2 shales (0.89 wt%) is also significantly elevated relative to Group 1 (0.18 wt%) and Group 3 (0.01 wt%) shales. Despite these observations, Group 2 shales of the Schwarzrand Subgroup record $\delta^{13}C_{carb\text{-}sh}$ values that are depleted relative to carbonates above and below the sampled shale package in section 3 and below the sampled shale package at section 4 (fig. 2). If seawater was the primary DIC source for carbonate cement precipitation in Group 2 shales, then the apparent deviation of $\delta^{13}C_{carb\text{-}sh}$ from approximately contemporaneous $\delta^{13}C_{carb}$ in sections 3 and 4 might be a consequence of contamination by additional ^{12}C associated with elevated TOC, and this is explored below.

The combined shale data from groups 1–3 show a significant positive correlation between $\delta^{13}C_{carb\text{-}sh}$ and $CaCO_3$ ($\rho = 0.69$, $p < 0.01$, fig. 4N), and a moderate but statistically significant negative correlation between $\delta^{13}C_{carb\text{-}sh}$ and TOC ($\rho = -0.43$, $p = 0.01$, fig. 4O). These correlations appear to support the inference that samples of lower purity (characterized by low $CaCO_3$/TOC, fig. 4P) will tend to record more negative $\delta^{13}C_{carb\text{-}sh}$. However, given the low TOC concentrations of shales from the Nama Group

(<0.20 wt%), the power of these statistical correlations are impacted to a degree by analytical uncertainties associated with TOC measurements (precision of better than ±0.04 wt%; Bowyer et al., 2020). Future studies that aim to further test this hypothesis would therefore benefit from sample sets with a larger range in TOC concentrations.

A carbonate to organic carbon concentration ratio of 7:1 has been suggested as a potential threshold below which the incorporation of ^{12}C from organic matter may result in deviation of bulk $\delta^{13}C$ from the composition of seawater DIC (Saltzman & Thomas, 2012). Indeed, very low $CaCO_3$/TOC ratios (0.06–0.36) in Group 3 shales may be partly responsible for the clearly depleted $\delta^{13}C_{carb\text{-}sh}$ relative to contemporaneous $\delta^{13}C_{carb}$ (fig. 4I). However, values of $\delta^{13}C_{carb\text{-}sh}$ in Group 1 shales clearly track the magnitude and trend of $\delta^{13}C_{carb}$ recorded by carbonate interbeds (fig. 2). These, after removing one outlier ($CaCO_3$/TOC = 84.99), have a mean $CaCO_3$/TOC of 3.70 (fig. 4D). The average purity of Group 2 shales (mean $CaCO_3$/TOC = 18.49, n = 12) is greater than Group 1 shales, even when this outlier value is included (mean = 11.83, n = 10, figs. 4D, H, P). It is therefore difficult to disregard values $\delta^{13}C_{carb\text{-}sh}$ derived from Group 2 shales, which are more negative than average $\delta^{13}C_{carb}$ of coeval carbonates in the Urusis Formation, on the basis of sample purity alone. We therefore explore the lithostratigraphic correlation of the Schwarzrand Subgroup in the vicinity of sections 3 and 4, in order to investigate the stratigraphic position of negative $\delta^{13}C_{carb\text{-}sh}$ data from Group 2 shales relative to regional $\delta^{13}C_{carb}$ chemostratigraphy.

5.4. Implications of alternative lithostratigraphic correlations for regional chemostratigraphy

The Urusis Formation in the Witputs Sub-basin is a mixed carbonate-siliciclastic succession deposited over a ca. 4-million-year period from ≤543 Ma to ≥538.5 Ma (Linnemann et al., 2019; Nelson et al., 2022; Saylor et al., 1998). Extensive studies of litho-, chemo-, bio- and sequence stratigraphy, alongside radiometric dating of the Urusis Formation succession, have focused on sections that outcrop on farms Nord Witputz 22, Swartpunt 74 and Swartkloofberg 95 (fig. 5; Darroch et al., 2015; Grotzinger et al., 1995; Jensen et al., 2000; Linnemann et al., 2019; Saylor & Grotzinger, 1996; Saylor et al., 1998; Wood et al., 2015). Confident lithostratigraphic correlation of strata in this region is complicated by laterally discontinuous outcrop associated with eroded topography, and the recognition of regional thrust faulting and folding associated with the Gariep Orogeny (fig. 5A; Saylor & Grotzinger, 1996). Here, we present four possible lithostratigraphic correlations for sections 1–4 (fig. 5B), which result in a range of possible chemostratigraphic correlations for the $\delta^{13}C_{carb-sh}$ data in section 4 relative to the radiometrically constrained Nama Group composite $\delta^{13}C_{carb}$ age framework. Each of these four lithostratigraphic correlations are discussed below.

Correlation 1 corresponds to the original lithostratigraphic correlation of Saylor and Grotzinger (1996) wherein the extended shale package at section 4 is correlated with the Feldschuhhorn Member (fig. 5B). This was justified by Saylor and Grotzinger (1996) on the basis of correlating an underlying unit of pink thrombolitic and stromatolitic lime mudstone at section 4 to a lithologically similar unit in the upper Huns Member at sections further to the east. According to this correlation, available radiometric data would constrain the negative $\delta^{13}C_{carb-sh}$ data recorded at section 4 to between 542.65 ± 0.15 Ma and 540.095 ± 0.099 Ma (Linnemann et al., 2019; Nelson et al., 2022), however the precise age and duration of the Feldschuhhorn Member within this interval remains uncertain. This is further complicated by reliability of available radiometric ages and uncertainty in lithostratigraphic correlation between sections 2 and 3.

Recent re-dating of an ash bed within section 2 preliminarily suggests that this section was deposited laterally equivalent to, rather than stratigraphically beneath, section 3 (Messori et al., 2021). This may be justified by the consistent lithostratigraphic architecture and identical number of ash beds between sections 2 and 3 (fig. 5B). If this is the case, section 2 was likely deposited in a shallower depositional environment than section 3 based on the available sedimentological details. The lithostratigraphic and radiometric correlation between sections 2 and 3 demands future clarification, as it has significant implications for the total thickness of the Urusis Formation in the Witputs Sub-basin, lithostratigraphic subdivision, and lateral differences in sedimentation rate. Differences in sedimentation rate between correlative sections also have significant implications for interpretations of associated geochemical proxy data (Nelson et al., 2022). Integrated stratigraphic, geochemical and radiometric dating may resolve these ongoing uncertainties.

Correlation 2 implies that the extended shale package at section 4 is equivalent to the transgressive systems tract of medium scale sequence E17 of Saylor (2003), which immediately underlies section 3. Given the uncertainty in lithostratigraphic correlation between sections 2 and 3, this would result in an age range for the section 4 $\delta^{13}C_{carb-sh}$ data equivalent to, or slightly younger than, correlation 1, but still ≥540.095 ± 0.099 Ma, if this is the accepted depositional age of the lowermost ash bed in section 3 (fig. 5B, but see Nelson et al., 2022). Alternatively, correlation 3 implies that the two extended shale packages in sections 3 and 4 are coeval, but were deposited at significantly different depositional rates, and that both are <538.99 ± 0.21 Ma (Linnemann et al., 2019).

Lastly, correlation 4 re-positions section 4 stratigraphically above section 3, and implies that the negative $\delta^{13}C_{carb-sh}$ data in section 4 are younger than the negative $\delta^{13}C_{carb-sh}$ data in section 3, <538.99 ± 0.21 Ma (fig. 5B; Linnemann et al., 2019). This correlation is consistent with the absence of tuff beds 0 to 5 from section 4, and tuff bed 6 from sections 2 or 3. Despite the recognition of thrust faulting in this area, this correlation is also the most parsimonious when considering the consistent regional dip to the northwest/west-northwest for sections to the east of the large NW−SE trending fold and fault system to the west of section 4 (figs. 5A and 6). Linnemann et al. (2019) note that tuff bed 6 may be reworked, and indeed if this reworking is from the underlying Spitskop Member (now removed by erosion), then the onset of the $\delta^{13}C_{carb-sh}$ excursion at section 4 may be younger than 538.6 Ma. A possible fifth stratigraphic correlation (not shown in fig. 5) would imply that the entire Feldschuhhorn Member at section 4 corresponds to ongoing deep water shale deposition equivalent to the entirety of the Feldschuhhorn and Spitskop members in shallower sections 1−3.

Correlation 4 may find further support in recent high resolution litho-, bio- and $\delta^{13}C_{carb}$ chemostratigraphic assessment, and radiometric dating of strata deposited in a correlative succession on the Neint Nababeep Plateau of the Vioolsdrif Sub-basin, northwest South Africa (Nelson et al., 2022). Figure 7 shows two possible litho- and chemostratigraphic correlations between all relevant sections of the Urusis and Nomtsas formations in the Witputs and Vioolsdrif sub-basins. In this figure, the lithostratigraphic correlation of Witputs Sub-basin sections follows correlation 4. The two lithostratigraphic correlations between the Witputs and Vioolsdrif sub-basins have different implications for rates of sediment accumulation in the Witputs sub-basin (fig. 8).

Nelson et al. (2022) interpret the age of ash bed 1 at section 3 as a maximum depositional age, and correlate the lower carbonate-dominated unit of the Neint Nababeep Plateau to the Huns Member (fig. 7). However, if ash beds 1–5 at section 3 approximate the ages of deposition, as originally proposed (Linnemann et al., 2019), then the implication is that the entire carbonate-dominated upper half of the composite Neint Nababeep Plateau succession is an expanded lateral equivalent to the Spitskop Member in the Witputs Sub-basin, rather than the entire Huns and Spitskop members (correlation 5 in figs. 7C, 8). This would further imply that, in the Neint Nababeep Plateau succession, time-equivalent deposits to the Huns Member are dominantly siliciclastic (correlation 5 in figs. 7C, 8). In this correlation, the lithostratigraphic architecture, $\delta^{13}C_{carb}$ -chemostratigraphy, and radiometric ages of the Neint Nababeep Plateau succession are all consistent with lateral correlation to sections 1–4, to the north, which were themselves deposited more slowly (correlation 5, figs. 7B, C, 8). Adopting correlation 4 for sections of the Witputs Sub-basin and either the original correlation of Nelson et al. (2022) or correlation 5 between the Witputs and Vioolsdrif sub-basins, also allows for basin-wide transgression and the contemporaneous development of pinnacle reefs of the lower Nomtsas Formation at section 4 and the Neint Nababeep Plateau (fig. 7C). This would, by extension, imply that the fragmented ash bed at section 4 (538.58 ± 0.19 Ma, Linnemann et al., 2019) is redeposited from the uppermost Spitskop Member. The veracity of correlation 5 requires future verification of the lithostratigraphic and radiometric correlation between sections 2 and 3 (e.g., Messori et al., 2021), particularly by integration of data from core with outcrop.

5.5. Calibrating $\delta^{13}C_{carb\text{-}sh}$ data within the current terminal Ediacaran age framework

Nelson et al. (2022) record relatively stable, positive $\delta^{13}C_{carb}$ values throughout the Neint Nababeep Plateau section, with scattered negative values that may be laterally correlative with negative $\delta^{13}C_{carb\text{-}sh}$ values at section 3, documented herein (figs. 8, 9). This may also imply that the magnitude of negative $\delta^{13}C_{carb\text{-}sh}$ in Group 2 shales at section 3 is exaggerated relative to contemporaneous $\delta^{13}C_{carb}$, possibly associated with sample impurity (Nelson et al., 2022). However, given the uncertainty in the lithostratigraphic correlation of section 4, it remains possible that $\delta^{13}C_{carb\text{-}sh}$ data recorded by Group 2 shales at section 4 reflect trends in seawater $\delta^{13}C_{DIC}$.

A composite chemostratigraphic curve for the Nama Group has been constructed via visual alignment of $\delta^{13}C_{carb}$ data within the well-established litho- and chemostratigraphic framework of the Kuibis and Schwarzrand subgroups, and temporally constrained by all available radiometric ages within and between sections (fig. 9, full details of the methodological approach and associated uncertainties are provided in Bowyer et al., 2022, 2023). Within this framework, three chemostratigraphic alignments for section 4 result from lithostratigraphic correlations 1 to 4 of the Urusis Formation in the Witputs Sub-basin, and correlation 5 between the Witputs and Vioolsdrif sub-basins (fig. 9). In lithostratigraphic correlations 1 and 2, radiometric ages of 542.65 Ma and 540.099 Ma that bracket deposition of (at maximum) the upper Nasep, Huns and Feldschuhhorn members (Linnemann et al., 2019; Nelson et al., 2022) may permit correlation of the $\delta^{13}C_{carb\text{-}sh}$ data at section 4 with the radiometrically-constrained negative $\delta^{13}C_{carb}$ excursion in the A4 Member of the Ara Group, Oman (figs. 9A–C; Bowring et al., 2007). By contrast, lithostratigraphic correlation 3 results in direct correlation between $\delta^{13}C_{carb\text{-}sh}$ data at sections 3 and 4 (fig. 9D). In this correlation, $\delta^{13}C_{carb\text{-}sh}$ values at section 4 are significantly depleted relative to $\delta^{13}C_{carb\text{-}sh}$ and $\delta^{13}C_{carb}$ at section 3, and cannot be considered informative of any trend in seawater $\delta^{13}C_{DIC}$.

The 1n/BACE has not been recorded in the Witputs or Vioolsdrif sub-basins (fig. 7), and associated radiometric data may therefore support a 1n/BACE onset after 538.04 ± 0.14 Ma (Nelson et al., 2022), consistent with age models C to F of Bowyer et al. (2022, 2023). If $\delta^{13}C_{carb\text{-}sh}$ values of Group 2 shales at section 4 approximate the magnitude and trend of seawater $\delta^{13}C_{DIC}$, then lithostratigraphic correlation 4 may suggest that the apparent negative $\delta^{13}C_{carb\text{-}sh}$ excursion recorded at section 4 is a possible candidate for the regional expression of the 1n/BACE (fig. 9E). Based on models C to F of Bowyer et al. (2022, 2023), the inferred duration of the 1n/BACE (prior to peak 2p) is ~2.5 Myr. This duration, in conjunction with correlation 4 (fig. 5B), also yields the slowest, and potentially most plausible, depositional rate (44 $mMyr^{-1}$) for the ~90 m-thick shale package at section 4, relative to correlations 1–3. The hypothesis that $\delta^{13}C_{carb\text{-}sh}$ data of

Group 2 shales at section 4 represent seawater composition is testable by future targeted $\delta^{13}C_{carb}$ analyses of the upper pinnacle reef unit and overlying carbonate unit at section 4. However, we note that lithostratigraphic correlation 4, whereby pinnacle reefs developed contemporaneously at section 4 and the Neint Nabebeep Plateau, remains possible even if the $\delta^{13}C_{carb\text{-}sh}$ values recorded at section 4 do not represent seawater composition.

5.6. Potential biostratigraphic considerations and future target intervals

A preliminary global biostratigraphy has been constructed for the Ediacaran-Cambrian transition, which calibrates first and last appearances of key fossils directly within the global $\delta^{13}C_{carb}$ chemostratigraphic age framework (fig. 9C–F; Bowyer et al., 2022, 2023). This age framework is undergoing continuous calibration with the publication of new data and lithostratigraphic considerations (Bowyer et al., 2023; Nelson et al., 2022; Topper et al., 2022), and may be a useful predictive tool for targeting uncertain intervals of the stratigraphic record for geochemical and paleontological sampling. For example, the output of each age framework allows visualization of the series of biotic first and last appearances across the 1n/BACE interval, and may help to inform targeted sampling of stratigraphic intervals in order to clarify temporal and spatial distributions of critical transitional biota.

The Bayesian age-depth model of Nelson et al. (2022) constrains ages for the last appearances of erniettomorphs and *Cloudina* in the Neint Nababeep Plateau composite section (fig. 9F), and also permits the calculation of uncertainties for each age. In contrast to Bayesian age-depth models, uncertainties in the precise ages of biotic first and last appearances are difficult to constrain by visual $\delta^{13}C_{carb}$ alignment alone, especially when considering local effects, including diagenesis, on regional $\delta^{13}C_{carb}$ variability. However, it is possible to make broad observations concerning the chemostratigraphic position of biotic first and last appearances relative to large magnitude $\delta^{13}C_{carb}$ excursions such as the 1n/BACE, if long-term trends in $\delta^{13}C_{carb}$ within each succession reflect changes in global seawater $\delta^{13}C_{DIC}$.

The first appearance of the cloudinid *Zuunia chimidtsereni* in the Zuun-Arts Formation of the Zavkhan Terrane, Mongolia pre-dates negative $\delta^{13}C_{carb}$ values associated with the regional expression of the 1n/BACE (Topper et al., 2022). Visual

$\delta^{13}C_{carb}$ alignment of the Zavkhan and Nama Group successions, with associated uncertainties, permit a degree of temporal overlap between the maximum first appearance of *Z. chimidtsereni* and the last appearance of *Cloudina* in the Nama Group (fig. 9F; Bowyer et al., 2023). Similarly, a conservative maximum age for the first appearance of morphologically simple anabaritids in Siberia is set by fossils assigned to *Cambrotubulus* within the Turkut Formation of the Olenek Uplift, which stratigraphically underlie the onset of a negative $\delta^{13}C_{carb}$ excursion interpreted to correlate with the 1n/BACE (fig. 9F; Bowyer et al., 2023; Pelechaty et al., 1996; Rogov et al., 2015).

The maximum age for the onset of the 1n/BACE may approximate the termination of carbonate deposition in the Vioolsdrif Sub-basin of the Neint Nababeep Plateau (Bowyer et al., 2022, 2023; Nelson et al., 2022). Notwithstanding possible issues associated with deviation of the Nama Group $\delta^{13}C_{carb}$ record from the composition of seawater $\delta^{13}C_{DIC}$, and/or endemism associated with the record of Cambrian skeletal fossils, this age framework suggests that skeletal fossils that have commonly been associated with the Fortunian Stage of the lower Cambrian (e.g., morphologically simple anabaritids), or terminal Ediacaran tubular fossils that predate or coincide with the 1n/BACE in Laurentia (e.g., Selly et al., 2020), may yet be identified within the youngest interbedded carbonate-siliciclastic units of the Nama Group. According to lithostratigraphic correlation 4, herein, strata of the lower Nomtsas Formation in section 4 and the Neint Nababeep Plateau composite section, warrant continued, focused paleontological study.

6. CONCLUSIONS

We present new $\delta^{13}C_{carb-sh}$ and $\delta^{18}O_{carb-sh}$ data from carbonate cements within 107 shale samples of the terminal Ediacaran Nama Group, Namibia. These data are compared with the published $\delta^{13}C_{carb}$ and $\delta^{18}O_{carb}$ record derived from interbedded and laterally coeval carbonates throughout the Nama Group succession. Our preliminary results suggest that $\delta^{13}C_{carb-sh}$ recorded by samples deposited within mixed carbonate-clastic settings can approach $\delta^{13}C_{carb}$ if $CaCO_3$/TOC is sufficiently elevated. By contrast, shale samples with low $CaCO_3$/TOC deposited in clastic-only settings record values of $\delta^{13}C_{carb-sh}$ that are significantly depleted relative to $\delta^{13}C_{carb}$ in coeval carbonate-clastic successions. Intervals of the Nama Group succession characterized by both $\delta^{13}C$-$\delta^{18}O$ covariation and depleted $\delta^{13}C$ values appear to be restricted to those stratigraphic units and shallower facies that were more susceptible to mixing with meteoric fluids during early diagenesis. Recognition of these regional diagenetic effects permits a more accurate and detailed assessment of regional and global $\delta^{13}C_{carb}$ chemostratigraphy.

Despite these observations, the utility of $\delta^{13}C_{carb\text{-}sh}$ to infill gaps in the existing $\delta^{13}C_{carb}$ record remains unclear, even when using shale samples with high $CaCO_3$/TOC that were deposited in carbonate-clastic settings. For example, in the Nama Group, shale samples of the upper Schwarzrand Subgroup of the Witputs Sub-basin with elevated $CaCO_3$/TOC ratios record values of $\delta^{13}C_{carb\text{-}sh}$ that appear depleted relative to $\delta^{13}C_{carb}$ from underlying and overlying carbonate rocks. Robust comparison of $\delta^{13}C_{carb\text{-}sh}$ and $\delta^{13}C_{carb}$ between sections in this interval is also impaired by the recognition of several possible lithostratigraphic correlations for key sections of the upper Schwarzrand Subgroup. The most parsimonious lithostratigraphic alignment for this interval appears to support the synchronous development of carbonate pinnacle reefs in the Witputs and Vioolsdrif sub-basins of the Nama Group, associated with a major flooding (transgressive) event. This alignment may also result in temporal overlap of new $\delta^{13}C_{carb\text{-}sh}$ data in one section of the Witputs Sub-basin with the 1n/BACE, and warrants future targeted paleontological, geochemical and stratigraphic study.

ACKNOWLEDGMENTS

We acknowledge funding from UKRI grant NE/T008458/1 and Beca de Doctorado en el Extranjero, Becas Chile from ANID. We thank C. Chilcott, G. Sim, H. Mocke, C. Hoffmann, A. and S. Horn, U. Schulze Neuhoff, C. Husselman, B. Romer and L. Gessert. We thank two anonymous reviewers, Chris Jones, Associate Editor Tim Lyons and Editor Noah Planavsky for thorough and thoughtful comments that helped to significantly improve this manuscript. For the purpose of open access, the authors have applied a Creative Commons Attribution (CC BY) license to any Author Accepted Manuscript version arising.

APPENDIX

$CaCO_3$ concentration

Our calcium carbonate content estimates are based on the principle that the amount of $CaCO_3$ within a sample is directly proportional to the CO_2 gas produced when measuring carbon isotopic ratios. This implies that the wt% $CaCO_3$ can be calculated with the peak height areas reported by the Elementar PRECISION mass spectrometer using a simple linear regression model with intercept 0.

We used a powdered coral laboratory standard (COR1D, assumed 100% $CaCO_3$ content), which was run as a sample on the same days as the study samples. The COR1D results informed our model and permitted us to obtain regression equations to estimate wt% $CaCO_3$ for each of our shale samples. The error associated to the regression model, that combined all the measurements of the coral laboratory standard, was 0.88%. This error is the share of the variation that couldn't be explained by variation of standard sample weights ($1-R^2$).

To corroborate our estimates, we analysed five shale samples ranging from 0.008 to 15.51 wt% $CaCO_3$, using a colorimeter. The results are presented in table A2, below.

TABLE A2: COLORIMETER RESULTS AND % $CaCO_3$ ESTIMATES

Sample	Sample Mass (mg)	Mass Carbon (µg)	$CaCO_3$ (wt%)	IC (wt%)	Estimated $CaCO_3$ (wt%)	Difference (wt %)
ARS 4/3 1	31.2	898.52	14.40	2.88	15.51	1.102624
ARS 4/3 2	23.85	688.84	14.44	2.89		
ARS 4/3 3	30.13	866.64	14.38	2.88		
		Mean	**14.41**			
		RSD (%)	**0.21**			
OMK 3/12	34.50	123.42	1.789	0.36	3.052	1.263
SK1/4	41.70	1.80	0.022	0.00	0.008	0.014
SK1/9	33.66	78.00	1.159	0.23	1.421	0.263
DV2-8	61.74	25.54	0.207	0.04	0.230	0.023

Statistical Tests

To assess possible covariation between carbon and oxygen isotopes, $CaCO_3$ and TOC concentrations, and $CaCO_3$/TOC ratios for the different sample categories analysed here, we use correlation coefficients to measure the strength and significance of associations, and r-squared (R^2) to test how well those associations fit within a linear relationship.

Pearson's correlation coefficient (r) is one of the most widely used tests due to its high statistical power. Values of r range from 0 to 1, with $r = 0$ indicating no association and $r = 1$ indicating a perfect correlation, with significant correlations indicated where $p \leq 0.05$. Pearson's correlation coefficient, however, is a parametric test for linear associations, so assumptions about the normality of the distribution of the variables, constant residual variability, and linearity need to be fulfilled to properly interpret the results.

When these assumptions are not met we use the non-parametric equivalent test of Spearman's rank correlation. Spearman's rank correlation coefficient (ρ) measures the strength of monotonic associations, that is any kind of association, and not only a linear relationship. Values of ρ range from 0 (no correlation) to 1 (a perfect correlation). Significant correlations are identified when $p \leq 0.05$.

To determine if the isotopic data, $CaCO_3$ and TOC concentrations, and $CaCO_3$/TOC ratios were normally distributed and to inform further statistical correlation analysis, a Shapiro-Wilk normality test was used on eight sample type categories; Group 1 shales ($n = 21$) and coeval carbonates ($n = 115$), Group 2 shales ($n=24$) and coeval carbonates ($n = 92$), Group 3 shales of the Zaris Sub-basin ($n = 62$) and coeval carbonates of the Witputs Sub-basin ($n = 531$), all carbonates with $\delta^{13}C$ and $\delta^{18}O$ data ($n = 1029$), and all shales ($n = 107$). This test was chosen because it is considered to be appropriate for relatively small sample sizes (<100) and has a high statistical power for large sample sizes (Razali and Wah, 2011).

TABLE A3: SHAPIRO-WILK NORMALITY TEST

Sample Category	δ ^{13}C		δ^{18}O		*$CaCO_3$ Content*		*TOC Content +*		*$CaCO_3$/TOC +*	
	W	p-value	W	p-value	W	p-value	W	p-value	W	p-value
All carbonates	0.9310	2.23x10^{-21}	0.9769	1.02x10^{-11}	NA	NA	NA	NA	NA	NA
Group 1 shales	0.9720	7.77x10^{-01}	0.9703	7.40x10^{-01}	0.5750	1.08x10^{-06}	0.9203	3.59x10^{-01}	0.4774	1.98x10^{-06}
Carbonates interbedded with group 1 shales	0.9748	2.88x10^{-02}	0.9890	4.80x10^{-01}	NA	NA	NA	NA	NA	NA
Group 2 shales	0.9212	6.21x10^{-02}	0.9398	1.62x10^{-01}	0.8385	1.35x10^{-03}	0.6757	4.96x10^{-04}	0.8837	9.78x10^{-02}
Carbonates coeval with group 2 shales	0.9537	2.50x10^{-03}	0.9061	6.25x10^{-06}	NA	NA	NA	NA	NA	NA
Group 3 shales	0.9892	8.62x10^{-01}	0.9062	1.75x10^{-04}	0.3745	3.43x10^{-14}	0.8541	6.50x10^{-02}	0.6801	1.34x10^{-03}
Carbonates coeval with Group 3 shales (Witputs Sub-basin)	0.9234	8.51x10^{-16}	0.9395	7.22x10^{-14}	NA	NA	NA	NA	NA	NA
All shales	0.9872	3.99x10^{-01}	0.9426	1.64x10^{-04}	0.3984	1.52x10^{-18}	0.8095	6.17x10^{-05}	0.6367	2.11x10^{-07}

$^{+}$Sample size in this category is ≤12, causing the Shapiro-Wilk test to have low statistical power that may not detect deviation from normality.

In the Shapiro-Wilk test, the null hypothesis (H_0) is that the distribution of the isotopic data is normal and is rejected when a p-value is ≤0.05. Rejecting H_0 implies that the distribution of the data is very unlikely to have been randomly sampled from a normally distributed population. W is the test statistic of the Shapiro-Wilk test that summarizes if the data, when ordered and standardized in quantiles, fits standard normal quantiles, and it is intended to test the null hypothesis.

In consideration of the reported p-values, the H_0 was rejected for the carbon isotope data of all carbonates (including carbonates coeval to shale samples from Groups 1 to 3), and so the non-parametric test of Spearman's rank correlation (ρ) was chosen to assess possible correlations between the δ^{13}C and δ^{18}O of all carbonate groupings. Likewise, the null hypothesis was rejected based on the p-values associated with the $CaCO_3$ concentrations of all shale groups, pointing to the absence of a normal distribution of these data, and informing the more appropriate use of Spearman's rank correlation. Graphical examinations of data distribution with probability density distribution plots and quantile-quantile plots support these assessments. Considering the small sample sizes of shales with TOC and $CaCO_3$/TOC ratios, the interpretations of normality were assessed through use of probability density distribution plots and quantile-quantile plots. These suggested that TOC from Group 1 and Group 2 shales, and $CaCO_3$/TOC ratios from Group 1 and Group 3 shales were not normally distributed, thereby informing the appropriate use of Spearman's rank correlation coefficient.

Based on the Shapiro-Wilk test (table A3), and aforementioned graphical assessment, a normally distributed sample population was assumed for $\delta^{13}C$ and $\delta^{18}O$ of Group 1 and Group 2 shales, $CaCO_3$/TOC of Group 2 shales, and TOC of Group 3 shales. In these cases, the use of Pearson's correlation coefficient (r) was evaluated. By definition, Pearson's correlation coefficient measures the linear relationship between two variables and therefore relies on the residuals of the model to be normally distributed and have a constant variance. The Shapiro-Wilk test was performed on the residuals between the correlation of said variables to test for a normal distribution of their residuals (table A4).

To assess if the variance of the residuals of these correlations were constant, a Breusch-Pagan test was performed. This formal test uses a chi-squared distribution to test if the residuals, or the errors of the regression, depend on the explanatory variable of the model. When the Breusch-Pagan test returns a p-value <0.05, it implies non-constant errors that do not meet the conditions to use Pearson's correlation (table A4).

Based on the results of the Shapiro-Wilk and Breusch-Pagan tests, the null hypothesis of residuals having a normal distribution and constant variance, respectively, could not be rejected. Therefore, Pearson's correlation coefficient was chosen to assess associations between $\delta^{13}C$ and $\delta^{18}O$ of Group 1 and Group 2 shales, $CaCO_3$/TOC of Group 2 shales, and TOC of Group 3 shales (fig. 4A, 4E, 4K and 4H).

TABLE A4: SHAPIRO-WILK TEST AND BREUSCH-PAGAN TEST ON CORRELATION RESIDUALS

Sample Category	Test	$\delta^{18}O$ vs. $\delta^{13}C$ correlation		TOC vs. $\delta^{13}C$ correlation		$CaCO_3$/TOC vs. $\delta^{13}C$ correlation	
		Statistic	p-value	Statistic	p-value	Statistic	p-value
Group 1 shales	Shapiro-Wilk	0.9299	1.37×10^{-1}	NA	NA	NA	NA
	Breusch-Pagan	0.1190	7.30×10^{-1}	NA	NA	NA	NA
Group 2 shales	Shapiro-Wilk	0.918	5.26×10^{-2}	NA	NA	0.8857	1.04×10^{-1}
	Breusch-Pagan	0.0038	9.51×10^{-1}	NA	NA	0.2886	5.91×10^{-1}
Group 3 shales	Shapiro-Wilk	NA	NA	0.9438	5.97×10^{-1}	NA	NA
	Breusch-Pagan	NA	NA	2.5336	1.11×10^{-1}	NA	NA

Note: In each Breusch-Pagan test, the degree of freedom was 1.

TABLE A1. GEOCHEMICAL DATA FROM SHALES

Sample ID	Location[$] Latitude (°S)	Location[$] Longitude (°E)	Section height* (m)	$\delta^{13}C$ (‰)	$\delta^{18}O$ (‰)	$CaCO_3$ content (%)	TOC (wt%)	Age[+] (Ma)			
Group 2 shales (Extended shale packages within carbonate-clastic successions)											
<u>Zwartmodder - Section 8</u>											
Kuibis Subgroup, Dabis Formation, Kanies Member											
SWM2-3	24°53'40.98"	16°19'31.02"	15.50	-6.21	-12.93	0.81	0.056	550.25			
SWM2-2	24°53'40.98"	16°19'31.02"	10.50	-7.18	-13.68	0.18	0.062	550.37			
SWM2-1	24°53'40.98"	16°19'31.02"	03.00	-2.38	-13.15	1.66	0.045	550.55			
<u>Swartpunt - Section 3</u>											
Schwarzrand Subgroup, Urusis Formation, Spitskop Member											
SWP-18-33	27°28'25.98"	16°41'45.12"	76.10	-2.80	-6.11	1.16	N.D.[#]	538.78			
SWP-18-32	27°28'25.98"	16°41'45.12"	72.60	-0.51	-3.08	0.72	N.D.[#]	538.88			
SWP-18-31	27°28'25.98"	16°41'45.12"	71.60	-2.84	-5.57	1.88	N.D.[#]	538.91			
SWP-18-30	27°28'25.98"	16°41'45.12"	70.60	-8.52	-8.19	0.10	N.D.[#]	538.94			
SWP-18-29	27°28'25.98"	16°41'45.12"	69.60	-3.13	-4.31	1.15	N.D.[#]	538.97			
SWP-18-28	27°28'25.98"	16°41'45.12"	68.60	-2.88	-6.61	0.44	N.D.[#]	538.99			
SWP-18-27	27°28'25.98"	16°41'45.12"	67.30	-3.80	-7.89	0.22	N.D.[#]	539.03			
SWP-18-26	27°28'25.98"	16°41'45.12"	66.80	-5.33	-8.11	0.10	N.D.[#]	539.05			
SWP-18-25	27°28'25.98"	16°41'45.12"	66.30	0.17	-4.01	0.76	N.D.[#]	539.06			
SWP-18-24	27°28'25.98"	16°41'45.12"	65.50	-2.54	-7.44	0.25	N.D.[#]	539.08			
SWP-18-23	27°28'25.98"	16°41'45.12"	64.50	-3.98	-6.96	0.09	N.D.[#]	539.11			
SWP-18-22	27°28'25.98"	16°41'45.12"	63.50	-1.79	-9.85	1.65	N.D.[#]	539.14			
<u>Swartkloofberg - Section 4</u>											
Schwarzrand Subgroup, Urusis Formation, after correlations 1 to 3 (all samples are herein reassigned to the Feldschuhhorn Mb in correlation 1, and Spitskop Mb in correlation 3. Member assignment of correlation 2 depends upon confident lithostratigraphic correlation between sections 2 and 3). All samples reassigned to Nomtsas Fm after correlation 4.											
								Corr. 1	Corr. 2	Corr. 3	Corr. 4
SK1/10	27°26'48.24"	16°33'43.62"	89.00	-0.40	-7.38	1.67	0.092	540.10	540.10	538.78	535.47
SK1/9	27°26'48.24"	16°33'43.62"	75.00	-3.28	-4.76	1.42	0.073	540.26	540.26	538.84	535.79
SK1/8	27°26'48.24"	16°33'43.62"	47.75	-7.25	-6.33	0.99	0.071	540.57	540.57	539.95	536.41
SK1/7	27°26'48.24"	16°33'43.62"	44.55	-8.12	-6.61	0.97	0.093	540.61	540.61	539.96	536.48
SK1/6	27°26'48.24"	16°33'43.62"	34.95	-7.14	-9.96	1.57	0.193	540.72	540.72	539.00	536.70
SK1/5	27°26'48.24"	16°33'43.62"	23.75	-7.79	-6.99	4.43	0.081	540.85	540.85	539.05	536.95
SK1/4	27°26'48.24"	16°33'43.62"	15.75	-2.99	-8.64	0.01	0.069	540.94	540.94	539.08	537.14
SK1/3	27°26'48.24"	16°33'43.62"	10.15	-7.33	-8.88	0.02	0.072	541.00	541.00	539.10	537.26
SK1/1	27°26'48.24"	16°33'43.62"	1.50	-1.97	-7.89	2.91	0.068	541.10	541.10	539.14	537.46
Group 1 shales (Meter-scale shale interbeds within carbonate-clastic successions)											
<u>Arasab - Section 6</u>											
Kuibis Subgroup, Dabis Formation, Kliphoek Member											
ARS4/12	26°57'48.54"	16°27'25.98"	74.10	0.72	-6.19	0.12	N.D.[#]	549.91			
ARS4/11	26°57'48.54"	16°27'25.98"	66.70	-4.19	-13.63	0.05	N.D.[#]	549.94			
ARS4/10	26°57'48.54"	16°27'25.98"	64.10	-0.14	-7.22	0.97	N.D.[#]	549.95			
ASR4/9	26°57'48.54"	16°27'25.98"	63.10	-4.29	-12.30	0.05	N.D.[#]	549.96			
ARS4/7	26°57'48.54"	16°27'25.98"	38.10	2.50	-2.85	0.09	0.059	550.07			

Kuibis Subgroup, Dabis Formation, Mara Member								
ARS4/5	26°57'48.54"	16°27'25.98"	20.80	-1.77	-5.39	57.54	N.D.#	550.15
ARS4/6	26°57'48.54"	16°27'25.98"	22.20	-2.66	-12.19	0.05	0.086	550.15
ARS4/3	26°57'48.54"	16°27'25.98"	06.50	-2.65	-12.82	15.51	N.D.#	550.23
ARS4/2	26°57'48.54"	16°27'25.98"	2.60	-1.05	-3.72	80.03	N.D.#	550.25
ARS4/1	26°57'48.54"	16°27'25.98"	1.60	-0.94	-3.18	63.83	N.D.#	550.25
Omkyk - Section 9								
Kuibis Subgroup, Zaris Formation, Upper Omkyk Member								
OMK4/1	24°48'19.02"	16°13'45.00"	73.00	1.92	-9.58	0.02	0.040	549.50
Kuibis Subgroup, Zaris Formation, Lower Omkyk Member								
OMK3/14	24°48'19.02"	16°13'45.00"	44.00	-1.87	-7.36	4.71	0.055	549.76
OMK3/13	24°48'19.02"	16°13'45.00"	39.00	1.30	-8.82	11.96	N.D.#	549.80
OMK3/12	24°48'19.02"	16°13'45.00"	38.00	-0.50	-9.26	3.05	N.D.#	549.81
OMK3/11	24°48'19.02"	16°13'45.00"	28.20	1.30	-10.06	56.54	N.D.#	N.D.#
OMK3/10	24°48'19.02"	16°13'45.00"	23.50	1.07	-11.13	50.22	N.D.#	N.D.#
OMK3/9	24°48'19.02"	16°13'45.00"	22.00	-3.46	-5.78	0.49	0.076	N.D.#
OMK3/8	24°48'19.02"	16°13'45.00"	21.50	-4.41	-7.60	48.64	0.052	N.D.#
OMK3/7	24°48'19.02"	16°13'45.00"	17.00	-2.11	-9.48	0.17	N.D.#	549.97
OMK3/6	24°48'19.02"	16°13'45.00"	14.25	2.72	-10.38	41.78	N.D.#	N.D.#
OMK3/5	24°48'19.02"	16°13'45.00"	7.50	-4.36	-4.89	0.11	0.055	550.04
OMK3/4	24°48'19.02"	16°13'45.00"	6.50	-2.37	-12.43	11.66	N.D.#	550.05
OMK3/3	24°48'19.02"	16°13'45.00"	4.50	-2.10	-6.64	0.09	0.056	550.07
OMK3/2	24°48'19.02"	16°13'45.00"	3.00	0.91	-3.43	0.47	0.045	550.08
OMK3/1	24°48'19.02"	16°13'45.00"	2.00	0.59	-0.46	0.41	N.D.#	550.09
Brak – Section 10								
Kuibis Subgroup, Dabis Formation (equivalent to Kanies to lower Kliphoek members of Witputs Sub-basin)								
BRK2/16	23°58'16.98"	16°08'06.48"	140.00	1.75	-7.68	16.23	N.D.#	549.85
BRK2/15	23°58'16.98"	16°08'06.48"	90.00	-1.49	-4.53	0.11	N.D.#	550.33
BRK2-12	23°58'16.98"	16°08'06.48"	65.00	-7.25	-6.04	100.00	0.097	550.41
BRK2/11	23°58'16.98"	16°08'06.48"	60.00	-3.09	-7.29	0.18	0.108	550.43
BRK2/10	23°58'16.98"	16°08'06.48"	31.95	-5.39	-7.96	83.76	N.D.#	550.52
BRK2-9	23°58'16.98"	16°08'06.48"	31.80	-6.63	-7.99	0.60	0.070	550.52
BRK2/7	23°58'16.98"	16°08'06.48"	30.75	-5.40	-4.74	90.35	N.D.#	550.52
BRK2/6	23°58'16.98"	16°08'06.48"	30.60	-9.41	-4.39	90.44	0.261	550.52
Group 3 shales (clastic-only successions*)								
C14 Road Transect – section 12								
Schwarzrand Subgroup, Nomtsas Formation, Niep Member								
D860-21	24°34'58.98"	16°55'49.14"	2080.27	-8.89	-12.09	N.D.#	N.D.#	538.20
D860-20	24°28'47.04"	16°52'56.58"	2045.72	-11.73	-12.75	N.D.#	0.074	538.38
D860-19	24°26'49.68"	16°52'06.48"	2028.45	-12.90	-13.09	N.D.#	N.D.#	538.47
Schwarzrand Subgroup, Nomtsas Formation, Kreyrivier Member								
D860-18	24°25'24.60"	16°50'42.78"	2022.35	-11.41	-12.46	N.D.#	0.095	538.50
Schwarzrand Subgroup, Urusis Formation								
D860-17	24°25'24.60"	16°50'42.78"	1775.00	-7.39	-12.25	0.02	N.D.#	539.95
D850 Road Transect – section 12								
Schwarzrand Subgroup, Urusis Formation								
D850-1	24°40'53.52"	16°46'15.78"	1852.67	-12.26	-13.25	0.02	N.D.#	539.37
D850-3	24°38'33.66"	16°40'46.20"	1345.00	-6.25	-12.63	0.03	N.D.#	543.16

D850-5	24°37'54.36"	16°39'03.84"	1220.00	-7.64	-10.86	0.04	N.D.[#]	544.09
Schwarzrand Subgroup, Nomtsas Formation, Niep Member								
S15	24°42'56.22"	16°54'48.54"	2080.27	-13.29	-12.87	0.01	N.D.[#]	538.20
S14	24°41'16.68"	16°52'45.12"	2055.88	-12.11	-12.23	0.01	N.D.[#]	538.33
Schwarzrand Subgroup, Urusis Formation								
S13	24°40'49.08"	16°47'03.96"	1956.31	-13.24	-13.38	0.02	N.D.[#]	538.60
S12b	24°40'49.20"	16°44'17.10"	1775.45	-6.61	-11.62	0.02	N.D.[#]	539.95
S12a	24°40'49.20"	16°44'17.10"	1775.45	-12.47	-13.89	0.02	0.055	539.95
S11	24°39'35.52"	16°42'12.54"	1492.99	-13.02	-12.41	0.00	N.D.[#]	542.05
S10	24°37'54.54"	16°36'22.92"	1051.02	-8.22	-12.49	0.01	N.D.[#]	545.35
Schwarzrand Subgroup, Nudaus Formation, Vingerbreek Member								
S9	24°37'51.54"	16°33'23.16"	965.00	-9.23	-13.09	0.02	N.D.[#]	545.36
S7	24°34'06.72"	16°28'40.86"	930.00	-5.79	-11.53	0.01	0.102	545.57
S6	24°32'19.02"	16°26'21.30"	900.00	-10.37	-13.55	0.01	N.D.[#]	545.74
Schwarzrand Subgroup, Nudaus Formation, Niederhagen Member								
S5	24°29'50.76"	16°25'33.36"	870.00	-7.53	-12.09	0.02	N.D.[#]	545.92
S4	24°28'55.14"	16°23'11.94"	865.00	-5.05	-10.58	0.01	0.090	545.95
Kuibis Subgroup, Zaris Formation, Urikos Member								
S3	24°29'18.96"	16°20'30.12"	780.00	-8.33	-13.94	0.01	N.D.[#]	546.45
S2a	24°29'09.72"	16°19'13.92"	760.00	-4.15	-4.04	N.D.[#]	N.D.[#]	547.73
S1	24°29'09.72"	16°19'13.92"	680.00	-6.35	-10.56	0.00	0.079	548.05
<u>D860 Road Transect – section 12</u>								
Schwarzrand Subgroup, Urusis Formation								
D860-15	24°19'19.32"	16°47'40.92"	1374.12	-8.40	-13.84	0.01	N.D.[#]	542.94
D860-13	24°13'05.52"	16°51'15.72"	1315.00	-6.15	-12.15	0.03	N.D.[#]	543.38
D860-11	24°12'14.58"	16°50'46.20"	1200.00	-9.52	-13.19	0.01	N.D.[#]	544.24
D860-9	24°11'40.50"	16°50'32.22"	1157.70	-6.45	-12.67	0.01	0.099	544.55
D860-7	24°10'41.22"	16°51'56.34"	1080.48	-9.81	-13.79	0.02	N.D.[#]	545.13
Schwarzrand Subgroup, Nudaus Formation, Vingerbreek Member								
D860-5	24°10'09.90"	16°53'19.32"	950.00	-11.29	-14.08	0.01	N.D.[#]	545.45
Schwarzrand Subgroup, Nudaus Formation, Niederhagen Member								
D860-3	24°06'57.42"	16°58'21.54"	860.00	-10.57	-13.06	0.01	N.D.[#]	545.98
D860-1	24°05'54.90"	16°59'36.96"	780.00	-7.63	-12.07	0.01	N.D.[#]	546.45
<u>Driedoornvlakte south – section 11</u>								
Schwarzrand Subgroup, Nudaus Formation, Niederhagen Member								
DV2-23	23°53.028'	16°39.607'	660.00	-7.36	-14.41	0.01	N.D.[#]	545.93
DV2-24	23°52.763'	16°39.983'	640.00	-8.38	-9.96	0.07	N.D.[#]	546.14
DV2-25	23°52.665'	16°39.928'	624.00	-5.81	-13.55	0.02	N.D.[#]	546.31
DV2-26	23°52.663'	16°39.924'	622.00	-7.31	-12.38	0.02	N.D.[#]	546.33
DV2-27	23°52.641'	16°39.893'	615.00	-8.70	-11.66	0.01	N.D.[#]	546.40
Kuibis Subgroup, Zaris Formation, Urikos Member (above OS2 Unit 3m)								
DV2-28	23°53.028'	16°39.607'	580.00	-9.70	-12.74	0.01	N.D.[#]	546.46
DV2-22	23°52.763'	16°39.983'	557.00	-10.25	-12.44	0.00	N.D.[#]	547.24
DV2-21	23°52.665'	16°39.928'	555.00	-9.64	-15.72	0.01	0.091	547.31
DV5	23°52.663'	16°39.924'	550.00	-9.04	-11.39	0.01	N.D.[#]	547.48
DV4	23°52.641'	16°39.893'	548.00	-5.28	-6.91	0.56	N.D.[#]	547.55
DV3	23°52.490'	16°39.813'	538.00	-5.95	-11.24	0.01	N.D.[#]	547.89
DV2-30	23°52.624'	16°39.182'	534.00	-7.66	-10.00	0.00	N.D.[#]	548.02

DV2-29	23°52.624'	16°39.182'	532.00	-9.23	-12.28	0.01	N.D.[#]	548.09
DV2	23°52.590'	16°39.207'	530.00	-6.78	-11.42	0.01	N.D.[#]	548.16
DV1	23°52.583'	16°39.210'	528.00	-5.21	-9.31	0.03	N.D.[#]	548.23
DV2-31	23°52.574'	16°39.208'	510.00	-15.45	-14.95	0.00	N.D.[#]	548.84
Kuibis Subgroup, Zaris Formation, Urikos Member (down-dip equivalent to OS2 Unit 3m)								
DV2-20	23°52.338'	16°39.800'	470.00	-10.32	-11.87	0.01	0.093	548.91
DV2-19	23°52.338'	16°39.800'	460.00	-7.48	-11.32	0.01	0.093	548.93
Kuibis Subgroup, Zaris Formation, Urikos Member (down-dip equivalent to OS2 Unit 3i)								
DV2-18	23°52.542'	16°39.175'	450.00	-8.06	-12.72	0.01	N.D.[#]	548.94
Kuibis Subgroup, Zaris Formation, Urikos Member (down-dip equivalent to OS2 Unit 2m)								
DV2-15	23°52.530'	16°39.176'	310.00	-2.59	-6.67	1.45	N.D.[#]	549.21
DV2-16	23°52.369'	16°39.368'	310.00	-3.34	-7.75	0.01	N.D.[#]	549.21
Kuibis Subgroup, Zaris Formation, Urikos Member (down-dip equivalent to OS2 Unit 1b)								
DV2-14	23°52.113'	16°39.331'	230.00	-2.54	-6.50	0.57	N.D.[#]	549.36
DV2-8	23°51.499'	16°39.712'	230.00	-3.33	-9.44	0.23	N.D.[#]	549.36
DV2-13	23°51.488'	16°39.736'	185.00	-1.25	-8.60	2.83	N.D.[#]	549.44
DV2-7	23°51.475'	16°39.685'	179.00	-5.04	-11.27	0.01	N.D.[#]	549.46
DV2-6	23°51.474'	16°39.684'	172.00	-4.59	-11.36	0.21	N.D.[#]	549.47
DV2-12	23°51.440'	16°39.673'	170.00	-2.28	-7.61	0.54	N.D.[#]	549.47
Kuibis Subgroup, Zaris Formation, Urikos Member (down-dip equivalent to OS2 Unit 1a)								
DV2-11	23°51.439'	16°39.662'	163.00	-1.00	-7.72	2.34	N.D.[#]	549.49
DV2-10	23°51.429'	16°39.637'	120.00	-1.85	-6.94	3.16	N.D.[#]	549.57
DV2-9	23°51.416'	16°39.624'	120.00	-4.03	-11.76	0.02	N.D.[#]	549.57

Grey shading indicates samples that were interpreted as shale upon collection and herein reclassified as impure carbonate based on $CaCO_3$ content.

[$]Coordinates for bases of sampled sections (except in the case of samples from sections 11 and 12, where coordinates indicate the positions of individual sampling localities).

[+]Sample ages updated after Age Model D of Bowyer et al. (2022), with the exception of samples from section 4, where 4 alternative age models correspond to correlations 1 to 4 in fig. 5. Full updated age model after Bowyer et al. (2022) and Bowyer et al. (2023) available upon request.

*Sample heights in clastic-only successions based on estimated positions relative to total Nama Group thickness (Bowyer et al., 2020).

[#]N.D. = not determined.

REFERENCES

Ahm, A. S. C., Bjerrum, C. J., Blättler, C. L., Swart, P. K., & Higgins, J. A. (2018). Quantifying early marine diagenesis in shallow-water carbonate sediments. *Geochimica et Cosmochimica Acta*, *236*, 140-159.

Ahm, A.-S. C., Bjerrum, C. J., Hoffman, P. F., Macdonald, F. A., Maloof, A. C., Rose, C. V., Strauss, J. V., & Higgins, J. A. (2021). The Ca and Mg isotope record of the Cryogenian Trezona carbon isotope excursion. *Earth and Planetary Science Letters, 568*, 117002.

Ahm, A.-S., & Husson, J. (2022). Local and Global Controls on Carbon Isotope Chemostratigraphy. Cambridge University Press.

Allan, J. R., & Matthews, R. K. (1982). Isotope signatures associated with early meteoric diagenesis. *Sedimentology, 29*, 797-817.

Blanco, G., Germs, G. J. B., Rajesh, H. M., Chemale, F., Dussin, I. A., & Justino, D. (2011). Provenance and paleogeography of the Nama Group (Ediacaran to early Palaeozoic, Namibia): Petrography, geochemistry and U-Pb detrital zircon geochronology. *Precambrian Research, 187*, 15-32.

Blanco, G., Rajesh, H. M., Germs, G. J. B., & Zimmermann, U. (2009). Chemical composition and tectonic setting of chromian spinels from the Ediacaran-early Paleozoic Nama group, Namibia. *Journal of Geology, 117*, 325-341.

Boggiani, P. C., Gaucher, C., Sial, A. N., Babinski, M., Simon, C. M., Riccomini, C., Ferreira, V. P., & Faurchild, T. R. (2010). Chemostratigraphy of the Tamengo

Formation (Corumbá Group, Brazil): A contribution to the calibration of the Ediacaran carbon-isotope curve. *Precambrian Research, 182*, 382-401.

Bowring, S. A., Grotzinger, J. P., Condon, D. J., Ramezani, J., Newall, M. J., & Allen, P. A. (2007). Geochronologic constraints on the chronostratigraphic framework of the neoproterozoic Huqf Supergroup, Sultanate of Oman. *American Journal of Science, 307*, 1097-1145.

Bowyer, F. T., Shore, A. J., Wood, R. A., Alcott, L. J., Thomas, A. L., Butler, I. B., Curtis, A., Hainanan, S., Curtis-Walcott, S., Penny, A. M., & Poulton, S. W. (2020). Regional nutrient decrease drove redox stabilisation and metazoan diversification in the late Ediacaran Nama Group, Namibia. *Scientific Reports, 10*, 1-11.

Bowyer, F. T., Zhuravlev, A. Y., Wood, R. A., Shields, G. A., Curtis, A., Poulton, S. W., Condon, D. J., Yang, C., & Zhu, M. (2022). Calibrating the temporal and spatial dynamics of the Ediacaran-Cambrian radiation of animals. *Earth-Science Reviews, 103913*.

Bowyer, F. T., Zhuravlev, A. Y., Wood, R., Zhao, F., Sukhov, S. S., Alexander, R. D., Poulton, S. W., & Zhu, M. (2023). Implications of an integrated late Ediacaran to early Cambrian stratigraphy of the Siberian Platform, Russia. *Geological Society of America Bulletin*.

Brasier, M., Cowie, J., & Taylor, M. (1994). Decision on the Precambrian-Cambrian boundary stratotype. *Episodes, 17*, 3-8.

Canfield, D. E., Knoll, A. H., Poulton, S. W., Narbonne, G. M., & Dunning, G. R. (2020). Carbon isotopes in clastic rocks and the Neoproterozoic carbon cycle. *American*

Journal of Science, 320, 97-124.

Cochrane, D. J. W., Navarro, L., & Arnott, R. W. C. (2019). Sedimentological and geochemical evolution of an Ediacaran mixed carbonate-siliciclastic continental slope system, Windermere Supergroup, southern Canadian Cordillera, British Columbia, Canada. *Precambrian Research, 327*, 47-67.

Cramer, B. D., & Jarvis, I. (2020). Carbon isotope stratigraphy, *in* Gradstein, F. M., Ogg, J. G., Schmitz, M. D., and Ogg, G. M. eds., Geologic Time Scale 2020: Elsevier B.V., Amsterdam, p. 309-343.

Cui, H., Warren, L. V., Uhlein, G. J., Okubo, J., Liu, X. M., Plummer, R. E., Baele, J., Goderis, S., Claeys, P., & Li, F. (2020). Global or regional? Constraining the origins of the middle Bambuí carbon cycle anomaly in Brazil. *Precambrian Research, 348*, 105861.

Darroch, S. A. F., Sperling, E. A., Boag, T. H., Racicot, R. A., Mason, S. J., Morgan, A. S., Tweedt, S., Myrow, P., Johnston, D. T., Erwin, D. H., & Laflamme, M. (2015). Biotic replacement and mass extinction of the Ediacara biota. *Proceedings of the Royal Society B, 282*, 20151003.

Epstein, S., Buchsbaum, R., Lowenstam, H. A., & Urey, H. C. (1953). Revised carbonate-water isotopic temperature scale. *Geological Society of America Bulletin, 64*, 1315-1326.

Epstein, S., & Mayeda, T. (1953). Variations in O^{18} content of waters from natural sources. *Geochimica et Cosmochimica Acta, 4*, 213-224.

Germs, G. J. B. (1974). The Nama Group in South West Africa and Its Relationship to the Pan-African Geosyncline. *The Journal of Geology , 82*, 301-317.

Germs, G. J. B. (1983). Implications of a sedimentary facies and depositional environmental analysis of the Nama Group in South West Africa/Namibia. *Special Publications of the geological Society of South Africa, 11*, 89-114.

Germs, G. J. B., & Gresse, P. G. (1991). The foreland basin of the Damara and Gariep orogens in Namaqualand and southern Namibia: stratigraphic correlations and basin dynamics. *South African Journal of Geology, 94*, 159-169.

Geyman, E. C., & Maloof, A. C. (2019). A diurnal carbon cycle engine explains ^{13}C-enriched carbonates without increasing the global production of oxygen. *Proceedings of the National Academy of Sciences of the United States of America, 116*, 24433-24439.

Gresse, P. G., & Germs, G. J. B. (1993). The Nama foreland basin: sedimentation, major unconformity bounded sequences and multisided active margin advance. *Precambrian Research, 63*, 247-272.

Grotzinger, J. P., Bowring, S. A., Saylor, B. Z., & Kaufman, A. J. (1995). Biostratigraphic and geochronological constraints on early animal evolution. *Science, 13*, 229-272.

Halverson, G. P., Hoffman, P. F., Schrag, D. P., Maloof, A. C., & Rice, A. H. N. (2005). Toward a Neoproterozoic composite carbon-isotope record. *Geological Society of America Bulletin, 117*, 1181-1207.

Hodgin, E. B., Nelson, L. L., Wall, C. J., Barrón-Díaz, A. J., Webb, L. C., Schmitz, M. D., Fike, D. A., Hagadorn, J. W., & Smith, E. F. (2020). A link between rift-related volcanism and end-Ediacaran extinction? Integrated chemostratigraphy, biostratigraphy, and U-Pb geochronology from Sonora, Mexico. *Geology, 49*, 115-119.

Hoffman, P. F., & Lamothe, K. G. (2019). Seawater-buffered diagenesis, destruction of carbon isotope excursions, and the composition of DIC in Neoproterozoic oceans. *Proceedings of the National Academy of Sciences of the United States of America, 116*, 18874-18879.

Jensen, S., Saylor, B. Z., Gehling, J. G., & Germs, G. J. B. (2000). Complex trace fossils from the terminal Proterozoic of Namibia. *Geology, 28*, 143-146.

Khadka, M. B., Martin, J. B., & Jin, J. (2014). Transport of dissolved carbon and CO_2 degassing from a river system in a mixed silicate and carbonate catchment. *Journal of Hydrology, 513*, 391-402.

Kouchinsky, A., Bengtson, S., Pavlov, V., Runnegar, B., Torssander, P., Young, E., & Ziegler, K. (2007). Carbon isotope stratigraphy of the Precambrian-Cambrian Sukharikha River section, northwestern Siberian platform. *Geological Magazine, 114*, 1-10.

Linnemann, U., Ovtcharova, M., Schaltegger, U., Gärtner, A., Hautmann, M., Geyer, G., Vickers-Rich, P., Rich, T., Plessen, B., Hofmann, M., Zieger, J., Krause, R., Kriesfeld, L., & Smith, J. (2019). New high-resolution age data from the Ediacran-Cambrian boundary indicate rapid, ecologically driven onset of the Cambrian explosion. *Terra Nova, 31*, 49-58.

Maloney, K. M., Boag, T. H., Facciol, A. J., Gibson, B. M., Cribb, A., Koester, B. E., Kenchington, C. G., Racicot, R. A., Darroch, S. A. F., & Laflamme, M. (2020). Palaeoenvironmental analysis of Ernietta-bearing Ediacaran deposits in southern Namibia. *Palaeogeography, Palaeoclimatology, Palaeoecology, 556*, 109884.

Maloof, A. C., Porter, S. M., Moore, J. L., Dudás, F. Ö., Bowring, S. A., Higgins, J. A., Fike, D. A., & Eddy, M. P. (2010). The earliest Cambrian record of animals and ocean geochemical change. *Geological Society of America Bulletin, 122*, 1731-1774.

Melim, L. A., Westphal, H., Swart, P. K., Eberli, G. P., & Munnecke, A. (2002). Questioning carbonate diagenetic paradigms: Evidence from the Neogene of the Bahamas. *Marine Geology, 185*, 27-53.

Messori, F., Ovtcharova, M., Zieger, J., Geyer, G., Linnemann, U., Hofmann, M., & Vickers-Rich, P. (2021). New high precision U-Pb CA-ID-TIMS zircon ages from the Terminal Ediacaran in Namibia. *Goldschmidt*, July 2021 Abstracts with Programs.

Nelson, L. L., Ramezani, J., Almond, J. E., Darroch, S. A. F., Taylor, W. L., Brenner, D. C., Furey, R. P., Turner, M., & Smith, E. F. (2022). Pushing the boundary: A calibrated Ediacaran-Cambrian stratigraphic record from the Nama Group in northwestern Republic of South Africa. *Earth and Planetary Science Letters, 580*, 117396.

Parry, L. A., Boggiani, P. C., Condon, D. J., Garwood, R. J., Leme, J. de M., McIlroy, D., Brasier, M. D., Trindade, R., Capanha, G. A. C., Pacheco, M. L. A. F., Diniz, C. Q.

C., & Liu, A. (2017). Ichnological evidence for meiofaunal bilaterians from the terminal Ediacaran and earliest Cambrian of Brazil. *Nature Ecology and Evolution, 1*, 1455-1464.

Pelechaty, S. M., Kaufman, A. J., & Grotzinger, J. P. (1996). Evaluation of $\delta^{13}C$ chemostratigraphy for intrabasinal correlation: Vendian strata of northeast Siberia. *Geological Society of America Bulletin, 108*, 992-1003.

Razali, N. M., & Wah, Y. B. (2011). Power comparisons of shapiro-wilk, kolmogorov-smirnov, lilliefors and anderson-darling tests. *Journal of statistical modeling and analytics, 2*, 21-33.

Rodriguez Blanco, L., Eberli, G. P., Weger, R. J., Swart, P. K., Tenaglia, M., Rueda Sanchez, L. E., & McNeill, D. F. (2020). Periplatform ooze in a mixed siliciclastic-carbonate system - Vaca Muerta Formation, Argentina. *Sedimentary Geology, 396*, 105521.

Rogov, V. I., Karlova, G. A., Marusin, V. V., Kochnev, B. B., Nagovitsin, K. E., & Grazhdankin, D. V. (2015). Duration of the first biozone in the Siberian hypostratotype of the Vendian. *Russian Geology and Geophysics, 56*, 573-583.

Rooney, A. D., Cantine, M. D., Bergmann, K. D., Gómez-Pérez, I., Al Baloushi, B., Boag, T. H., Busch, J. F., Sperling, E. A., & Strauss, J. V. (2020). Calibrating the coevolution of Ediacaran life and environment. *Proceedings of the National Academy of Sciences of the United States of America, 117*, 16824-16830.

Saltzman, M. R., & Thomas, E. (2012). Carbon Isotope Stratigraphy, *in* Gradstein, F. M., Ogg, J. G., Schmitz, M. D., and Ogg, G. M. eds., *The Geological Time Scale 2012*:

Elsevier B.V., p. 1144.

Saylor, B. Z. (2003). Sequence stratigraphy and carbonate-siliciclastic mixing in a terminal Proterozoic foreland basin, Urusis Formation, Nama Group, Namibia. *Journal of Sedimentary Research, 73*, 264-279.

Saylor, B. Z., & Grotzinger, J. P. (1996). Reconstruction of important Proterozoic-Cambrian boundary exposures through the recognition of thrust deformation in the Nama Group of southern Namibia. *Communications of the Geological Survey of Namibia, 11*, 1-12.

Saylor, B. Z., Grotzinger, J. P., & Germs, G. J. B. (1995). Sequence stratigraphy and sedimentology of the Neoproterozoic Kuibis and Schwarzrand Subgroups (Nama Group), southwestern Namibia. *Precambrian Research, 73*, 153-171.

Saylor, B. Z., Kaufman, A. J., Grotzinger, J. P., & Urban, F. (1998). A composite reference section for terminal Proterozoic strata of southern Namibia. *Journal of Sedimentary Research, 68*, 1223-1235.

Schmitz, M. D. (2012). Radiogenic Isotope Geochronology, *in* Gradstein, F. M., Ogg, J. G., Schmitz, M. D., and Ogg, G. M. eds., *The Geological Time Scale 2012*: Elsevier, p. 115-126.

Selly, T., Schiffbauer, J. D., Jacquet, S. M., Smith, E. F., Nelson, L. L., Andreasen, B. D., Warren Huntley, J., Strange, M. A., O'Neil, G. R., Thater, C. A., Bykova, N., Steiner, M., Yang, B., & Cai, Y. (2020). A new cloudinid fossil assemblage from the terminal Ediacaran of Nevada, USA. *Journal of Systematic Palaeontology, 18*, 357-379.

Smith, O. (1999). Terminal Proterozoic carbonate platform development: stratigraphy and sedimentology of the Kuibis Subgroup (ca. 550–548 Ma), northern Nama Basin, Namibia: unpublished Masters dissertation, Massachusetts Institute of Technology.

Smith, E. F., Nelson, L. L., Strange, M. A., Eyster, A. E., Rowland, S. M., Schrag, D. P., & Macdonald, F. A. (2016). The end of the Ediacaran: Two new exceptionally preserved body fossil assemblages from Mount Dunfee, Nevada, USA. *Geology, 44*, 911-914.

Swart, P. K. (2015). The geochemistry of carbonate diagenesis: The past, present and future. *Sedimentology, 62*, 1233-1304.

Tarutani, T., Clayton, R. N., & Mayeda, T. K. (1969). The effect of polymorphism and Mg substitution on oxygen isotope fractionation between calcium carbonate and water. *Geochimica et Cosmochimica Acta, 33*, 987-996.

Topper, T., Betts, M. J., Dorjnamjaa, D., Li, G., Li, L., Altanshagai, G., Enkhbaatar, B., & Skovsted, C. B. (2022). Locating the BACE of the Cambrian: Bayan Gol in southwestern Mongolia and global correlation of the Ediacaran-Cambrian boundary. *Earth-Science Reviews, 229*, 104017.

Urey, H. (1947). The thermodynamic properties of isotopic substances. *Journal of the Chemical Society, 99*, 562-581.

Veizer, J., & Hoefs, J. (1976). The nature of $^{18}O/^{16}O$ and $^{13}C/^{12}C$ secular trends in sedimentary carbonate rocks. *Geochimica et Cosmochimica Acta, 40*, 1387-1395.

Wood, R., Bowyer, F., Penny, A., & Poulton, S. W. (2018). Did anoxia terminate

Ediacaran benthic communities? Evidence from early diagenesis. *Precambrian Research, 313*, 134-147.

Wood, R. A., Poulton, S. W., Prave, A. R., Hoffmann, K.-H., Clarkson, M. O., Guilbaud, R., Lyne, J. W., Tostevin, R., Bowyer, F., Penny, A. M., Curtis, A., & Kasemann, S. A. (2015). Dynamic redox conditions control late Ediacaran metazoan ecosystems in the Nama Group, Namibia. *Precambrian Research, 261*, 252-271.

Yang, C., Rooney, A. D., Condon, D. J., Li, X.-H., Grazhdankin, D. V., Bowyer, F. T., Hu, C., Macdonald, F., & Zhu, M. (2021). The tempo of Ediacaran evolution. *Science Advances, 7*, eabi9643.

Zhu, M. Y., Babcock, L. E., & Peng, S. C. (2006). Advances in Cambrian stratigraphy and paleontology: Integrating correlation techniques, paleobiology, taphonomy and paleoenvironmental reconstruction. *Palaeoworld, 15*, 217-222.

Zhu, M., Yang, A., Yuan, J., Li, G., Zhang, J., Zhao, F., Ahn, S. Y., & Miao, L. (2019). Cambrian integrative stratigraphy and timescale of China. *Science China Earth Sciences, 62*, 25-60.

FIGURE CAPTIONS

Fig. 1. (A) Geological map of the Nama Group with pins showing precise positions of sections discussed in the text. Map drafted using 1:250000 maps of Ai-Ais (Sheet 2716, 2010), Bethanien (Sheet 2616, 1999), Gibeon (Sheet 2516, 2000), Mariental (Sheet 2416, 2017), and Rehoboth (Sheet 2316, 2006), Geological Survey of Namibia, Ministry of Mines and Energy, and map of Neint Nababeep Plateau after Nelson et al. (2022). (B) Dominant lithology, interpreted facies and average paleocurrent directions for outcrop of the Kuibis Subgroup (≥550.5 to <547 Ma; after Germs, 1983). (C) Dominant lithology, interpreted facies, and average paleocurrent directions for outcrop of the Schwarzrand Subgroup (≥546 to <538 Ma; after Germs, 1983).

Fig. 2. Lithostratigraphy and chemostratigraphy of sections discussed in the text, including those sampled for $\delta^{13}C_{carb\text{-}sh}$ (subdivided into groups 1 to 3), with additional published $\delta^{13}C_{carb}$ data after Saylor et al. (1998), Smith (1999), Wood et al. (2015), Maloney et al. (2020), and Bowyer et al. (2022). Dated ash beds after Grotzinger et al. (1995, recalculated in Schmitz, 2012), Bowring et al. (2007), Linnemann et al. (2019), and Nelson et al. (2022). U.O. = Upper Omkyk Mb, Nud. = Nudaus Fm, Nom. = Nomtsas Fm, Mo. = Mooifontein Mb, Zar. = Zaris Fm, Nas. = Nasep Mb, Feld. = Feldschuhhorn Mb, Spitsk. = Spitskop Mb. Alternative correlations for sections 1 to 4, including correlations (1) and (4) shown for section 4, are discussed further in the text and figs. 5 to 7.

Fig. 3. Outcrop photographs of selected study sections and associated siliciclastic intervals. (A) Nonconformable contact between the Mesoproterozoic Kobos granite and

overlying mixed carbonate-siliciclastic sedimentary rocks of the lower Kuibis Subgroup at Farm Omkyk (section 9). (B) Group 1 samples. Decimeter to meter-scale shale interbeds in the mixed carbonate-clastic succession of the lower Omkyk Member (Zaris Formation) on Farm Omkyk (section 9). (C) Group 2 samples. Swartpunt (section 3) showing position of dated ash beds. Vertical dotted line demarks sampled shale interval. (D) Group 2 samples. Photograph showing position of extended shale package (vertical dotted line) sampled on Farm Swartkloofberg (section 4). Meter-sized fragments of ash bed 6 (Linnemann et al., 2019) occur above an erosional surface stratigraphically above the sampled interval (fig. 2). Normal fault recognized by Saylor and Grotzinger (1996) is noted in the right of the image. (E) Group 2 samples. Base of sampled siliciclastic interval on Farm Swartkloofberg (section 4). (F) Group 3 samples. Planate clastic succession constituting the Urikos Member of the Zaris Formation (foreground) shallowing up through the successions to the Nomtsas Formation (horizon), with increasing distance to the southeast. Photograph taken looking southeast from the Upper Omkyk Member at Farm Driedoornvlakte (section 11). (G) Group 3 samples. Example of shale-siltstone exposure from the clastic succession of the Schwarzrand Subgroup, Zaris Sub-basin. Digging was required to retrieve fresh material at each site.

Fig. 4. (A), (E), (I), (M): $\delta^{18}O$ versus $\delta^{13}C$ for Group 1 shales and associated interbedded carbonates (A), Group 2 shales and associated carbonates (E), Group 3 shales and contemporaneous carbonates of the Witputs Sub-basin (I), and all studied shales and carbonates (M). Solid grey trend lines and statistical data are for carbonate samples, whereas dashed black trend lines and statistical data are for shale samples. (B), (F), (J), (N): $CaCO_3$ content versus $\delta^{13}C_{carb\text{-}sh}$ for Group 1 shales (B), Group 2 shales (F), Group 3

shales (J), and all studied shales (N). (C), (G), (K), (O): TOC versus $\delta^{13}C_{carb-sh}$ for Group 1 shales (C), Group 2 shales (G), Group 3 shales (K), and all studied shales (O). (D), (H), (L), (P): $CaCO_3$/TOC versus $\delta^{13}C_{carb-sh}$ for Group 1 shales (D), Group 2 shales (H), Group 3 shales (L), and all studied shales (P). Horizontal dashed lines in (D), (H), (L), and (P) mark the 7:1 threshold ratio of $CaCO_3$/TOC (after Saltzman and Thomas, 2012). Note that the x-axis of all panels correspond to $\delta^{13}C$. All data symbols are colored according to approximate age, based on chemostratigraphic age model of Bowyer et al. (2022) updated with lithostratigraphic observations herein.

Fig. 5. Possible lithostratigraphic correlations for sections of the Urusis Fm in the Witputs Sub-basin on farms Swartkloofberg, Swartpunt and Nord Witputz. (A) Geological map showing locations of sections 1 to 4. Map redrawn from Saylor and Grotzinger (1996), with additional geological information from the 1:250000 map of AI-AIS (2716), Geological Survey of Namibia, Ministry of Mines and Energy. (B) Correlations 1–4, discussed in the main text. Corr. 1 follows original lithostratigraphic correlation of Saylor and Grotzinger (1996). Medium scale sequences C4 to E18 after Saylor (2003). Ash bed ages after Grotzinger et al. (1995, recalculated in Schmitz, 2012), Linnemann et al. (2019), and Nelson et al. (2022). Ash beds 0 and 6 are not considered useful for correlation (see text for details). Lithostratigraphic correlation between sections 2 and 3 remains uncertain after observations of Messori et al. (2021; see text for details). Correlation 4 implies that ash bed (6) is likely redeposited (Linnemann et al., 2019). Feld. = Feldschuhhorn Mb, Spitsk. = Spitskop Mb.

Fig. 6. (A) Inclined satellite image of strata that outcrop in the vicinity of sections 1 to 4 (GoogleEarth). See fig. 5A for coordinates and reoriented map. (B) Geological map of (A) modified and simplified after Saylor and Grotzinger (1996) and 1:250000 map of AI-AIS area (2716) Geological Survey of Namibia, Ministry of Mines and Energy. Colors of geological units correspond to key in figure 5A. (C), (D): Schematic cross-sections A–A' after possible lithostratigraphic correlations, following (C) correlation 1 of Saylor and Grotzinger (1996), and (D) correlation 4 (herein).

Fig. 7. (A) Simplified geological map of the Witputs and Vioolsdrif sub-basins to show positions of studied sections of the Urusis Formation (dashed red arrows are parallel to the hinge line of the possible flexural forebulge of the Koedoelaagte Arch after Germs & Gresse, 1991). (B) Litho- and chemostratigraphic correlation of study sections 1 to 4 in the Witputs Sub-basin, after correlation 4 (fig. 5B). Section information and data from Saylor et al. (1998), Wood et al. (2015), Bowyer et al. (2022) and this study. (C) Litho- and chemostratigraphic correlation of the composite Neint Nababeep Plateau section, showing Formation and Member subdivision after Nelson et al. (2022), and possible alternative subdivision of correlation 5, herein (see text for discussion). Ash bed ages after Grotzinger et al. (1995, recalculated in Schmitz, 2012), Linnemann et al. (2019), and Nelson et al. (2022). Ash beds 0 and 6 are not considered useful for correlation (see text for details). All sections to scale.

Fig. 8. Temporal calibration of litho-, bio- and chemostratigraphy between (A) Swartpunt (section 3) and (B) the Neint Nababeep Plateau composite section according to correlation 5. Colored horizontal bars show the lithostratigraphic positions of dated ash

beds used for calibration (ash beds 1-5: Swartpunt section; ash beds 7-11: Neint Nababeep Plateau). The age of each ash bed level is shown relative to the corresponding position within the uncertainty of each associated radiometric age (colored vertical bars). Ash beds 4 and 5 fall outside of analytical uncertainty, but within total uncertainty, of their associated radiometric ages. (C) $\delta^{13}C_{carb}$ chemostratigraphy between Swartpunt (section 3) and the Neint Nababeep composite section according to correlation 5. (D) The difference in sedimentation rate between Swartpunt (section 3) and the Neint Nababeep Plateau composite section that results from correlation 5, superimposed upon the modelled sedimentation rate for the Neint Nababeep Plateau composite section after Nelson et al. (2022). Key to litho- and biostratigraphy provided in figure 2. Radiometric ages are from Linnemann et al. (2019) and Nelson et al. (2022). $\delta^{13}C_{carb}$ data from Bowyer et al. (2022) and Nelson et al. (2022).

Fig. 9. Updated radiometrically-calibrated lithostratigraphic and $\delta^{13}C_{carb}$ chemostratigraphic age model for the Nama Group succession of Namibia and northwest South Africa (red data points) superimposed upon possible global $\delta^{13}C_{carb}$ age framework (grey circles after Model D of Bowyer et al., 2022) updated with new insight from the Siberian Platform, Russia (Bowyer et al., 2023), and Zavkhan Terrane, Mongolia (Topper et al., 2022). (A) Lithostratigraphic composite for the Zaris, Witputs and Vioolsdrif sub-basins. (B) Zircon U-Pb CA-ID-TIMS data from the Nama Group used in construction of this age framework, with associated internal/analytical uncertainty (Bowring et al., 2007; Linnemann et al., 2019; Nelson et al., 2022). (C) to (E): New $\delta^{13}C_{carb\text{-}sh}$ data from carbonate-clastic successions of the Nama Group, calibrated within the $\delta^{13}C_{carb}$ age framework to show the possible chemostratigraphic implications of alternative

lithostratigraphic correlations discussed herein (figs. 5–7). (F) Key global fossil first and last appearances calibrated within the resulting age framework. These occurrences are constrained directly within the $\delta^{13}C_{carb}$ age framework, and are independent of alternative correlations of $\delta^{13}C_{carb\text{-}sh}$ data. 1. FAD *Cloudina* in the Nama Group; 2. FAD soft-bodied fossils of the classic Nama assemblage in the Nama Group; 3. Maximum FAD of the cloudinid *Zuunia chimidtsereni* in the Zavkhan Terrane, Mongolia (Topper et al., 2022); 4. Minimum LAD of *Cloudina* in the Nama Group (538.47 Ma), calibrated within the Bayesian age-depth model of Nelson et al. (2022); 5. Minimum LAD erniettamorphs in the Nama Group (538.16 Ma), calibrated within the Bayesian age-depth model of Nelson et al. (2022); 6. Maximum FAD of *T. pedum* in the Nama Group (538.23 Ma), based on its absence from strata of the Neint Nababeep Plateau composite section; 7. Conservative estimate for maximum FAD of simple anabaritids (*Cambrotubulus*) in Siberia, after updated Siberian lithostratigraphic assessment and $\delta^{13}C_{carb}$ age model F of Bowyer et al. (2023). 8. Approximate age for LAD of the cloudinid *Zuunia chimidtsereni* in the Zavkhan Terrane, Mongolia (Topper et al., 2022) after age model F of Bowyer et al. (2023), and approximate age for FAD of *T. pedum* coincident with peak 2p in the Mount Dunfee section of Nevada (Smith et al., 2016). Key to lithostratigraphy provided in fig. 2. Member subdivision of the Zaris Sub-basin: 1 = Kanies, 2 = Omkyk, 3 = Hoogland, 4 = Urikos, 5 = Niederhagen, 6 = Vingerbreek, 7 = Kreyrivier, 8 = Niep. Member subdivision of the Witputs Sub-basin: 1 = Kanies, 2 = Mara, 3 = Kliphoek, 4 = Mooifontein, 5 = Niederhagen, 6 = Vingerbreek, 7 = Nasep, 8 = Huns, 9 = Feldschuhhorn, 10 = Spitskop. Acronyms BANE – 'basal Nama excursion', OME – 'Omkyk excursion', A0–A4, 1p, 1n/BACE and 2p correspond to named $\delta^{13}C_{carb}$ excursions (listed in full in Bowyer et al., 2022). Question marks denote uncertainty in global nature of isotope excursions A0 and A4.

1156 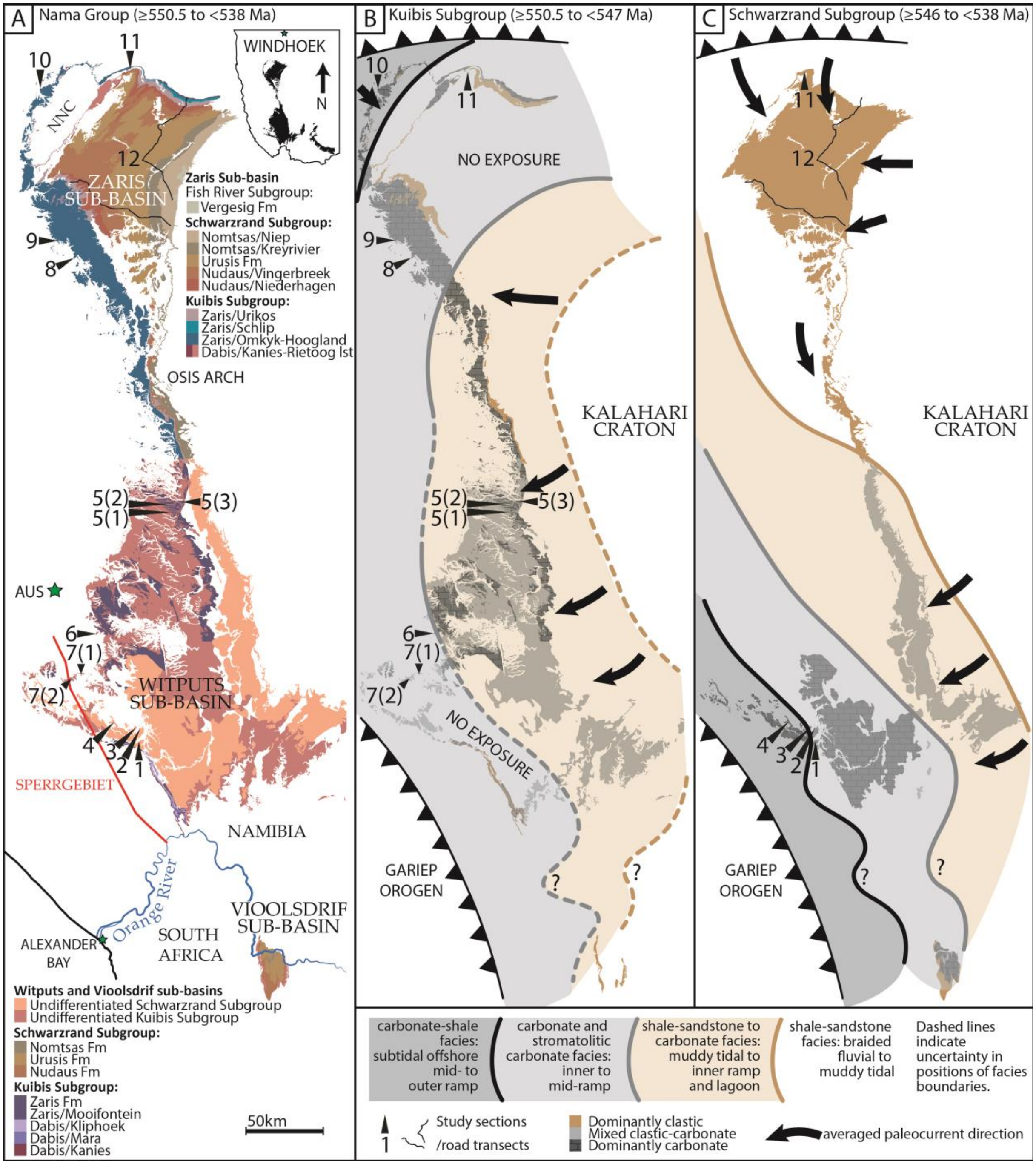
A Nama Group (≥550.5 to <538 Ma)
B Kuibis Subgroup (≥550.5 to <547 Ma)
C Schwarzrand Subgroup (≥546 to <538 Ma)
WINDHOEK
N
NNC
ZARIS SUB-BASIN
Zaris Sub-basin
Fish River Subgroup:
Vergesig Fm
Schwarzrand Subgroup:
Nomtsas/Niep
Nomtsas/Kreyrivier
Urusis Fm
Nudaus/Vingerbreek
Nudaus/Niederhagen
Kuibis Subgroup:
Zaris/Urikos
Zaris/Schlip
Zaris/Omkyk-Hoogland
Dabis/Kanies-Rietoog lst
OSIS ARCH
AUS
WITPUTS SUB-BASIN
SPERRGEBIET
NAMIBIA
Orange River
VIOOLSDRIF SUB-BASIN
ALEXANDER BAY
SOUTH AFRICA
Witputs and Vioolsdrif sub-basins
Undifferentiated Schwarzrand Subgroup
Undifferentiated Kuibis Subgroup
Schwarzrand Subgroup:
Nomtsas Fm
Urusis Fm
Nudaus Fm
Kuibis Subgroup:
Zaris Fm
Zaris/Mooifontein
Dabis/Kliphoek
Dabis/Mara
Dabis/Kanies
50km
NO EXPOSURE
KALAHARI CRATON
GARIEP OROGEN
carbonate-shale facies: subtidal offshore mid- to outer ramp
carbonate and stromatolitic carbonate facies: inner to mid-ramp
shale-sandstone to carbonate facies: muddy tidal to inner ramp and lagoon
shale-sandstone facies: braided fluvial to muddy tidal
Dashed lines indicate uncertainty in positions of facies boundaries.
Study sections /road transects
Dominantly clastic
Mixed clastic-carbonate
Dominantly carbonate
averaged paleocurrent direction

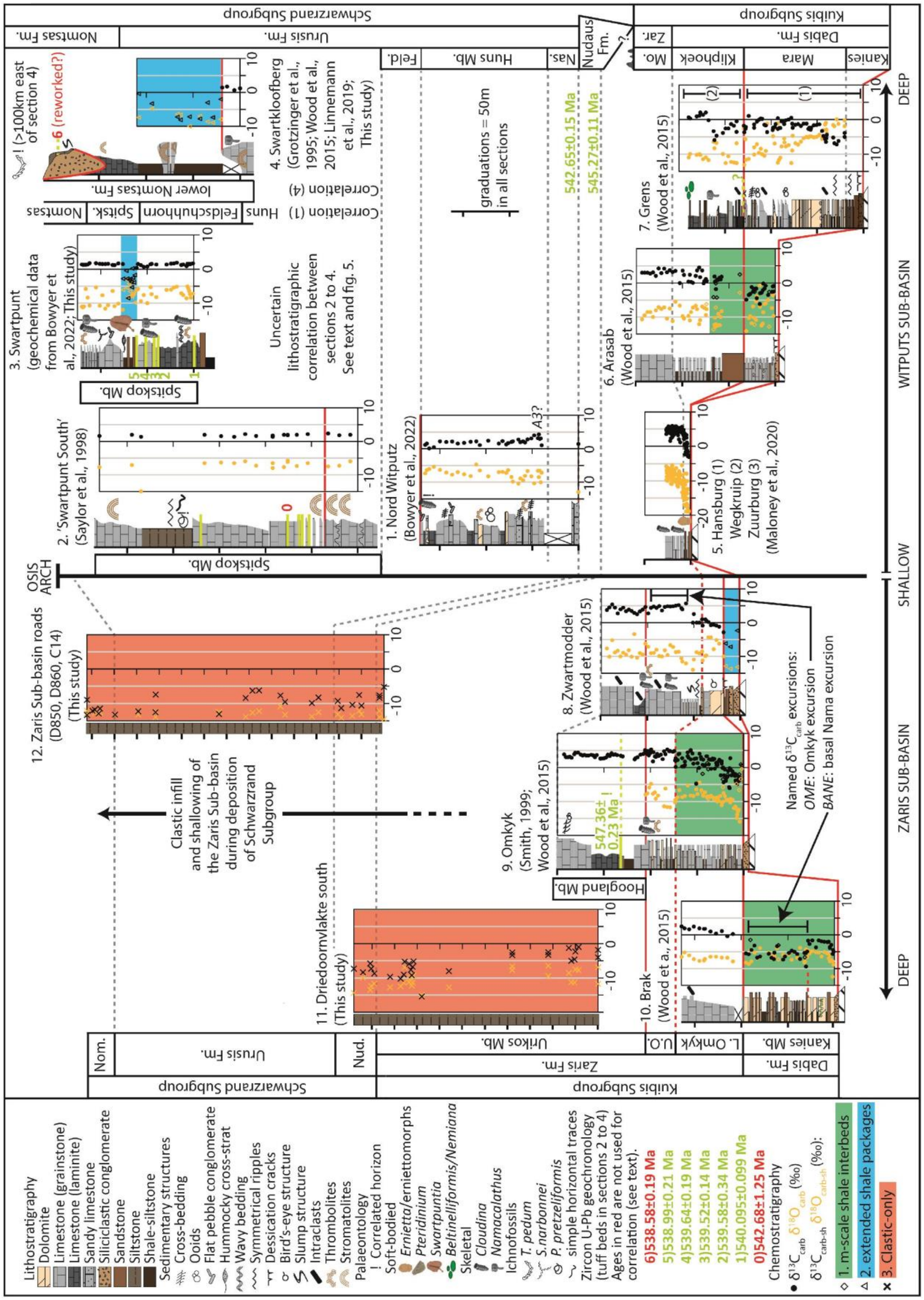

Lithostratigraphy
Dolomite
Limestone (grainstone)
Limestone (laminite)
Sandy limestone
Siliciclastic conglomerate
Sandstone
Siltstone
Shale-siltstone
Sedimentary structures
Cross-bedding
Ooids
Flat pebble conglomerate
Hummocky cross-strat
Wavy bedding
Symmetrical ripples
Dessication cracks
Bird's-eye structure
Slump structure
Intraclasts
Thrombolites
Stromatolites
Palaeontology
! Correlated horizon
Soft-bodied
Ernietta/erniettomorphs
Pteridinium
Swartpuntia
Beltinelliformis/Nemiana
Skeletal
Cloudina
Namacalathus
Ichnofossils
T. pedum
S.narbonnei
P. pretzeliformis
simple horizontal traces
Zircon U-Pb geochronology (tuff beds in sections 2 to 4). Ages in red are not used for correlation (see text).
6)538.58±0.19 Ma
5)538.99±0.21 Ma
4)539.64±0.19 Ma
3)539.52±0.14 Ma
2)539.58±0.34 Ma
1)540.095±0.099 Ma
0)542.68±1.25 Ma
Chemostratigraphy
1. m-scale shale interbeds
2. extended shale packages
3. Clastic-only
Schwarzrand Subgroup
Kuibis Subgroup
Nom.
Urusis Fm.
Nud.
Zaris Fm.
Urikos Mb.
U.O.
L. Omkyk
Dabis Fm.
Kanies Mb.
11. Driedoornvlakte south (This study)
10. Brak (Wood et a., 2015)
9. Omkyk (Smith, 1999; Wood et al., 2015)
547.36± 0.23 Ma !
Hoogland Mb.
12. Zaris Sub-basin roads (D850, D860, C14) (This study)
Clastic infill and shallowing of the Zaris Sub-basin during deposition of Schwarzrand Subgroup
8. Zwartmodder (Wood et al., 2015)
Named δ13Ccarb excursions:
OME: Omkyk excursion
BANE: basal Nama excursion
OSIS ARCH
DEEP
SHALLOW
ZARIS SUB-BASIN
WITPUTS SUB-BASIN
2. 'Swartpunt South' (Saylor et al., 1998)
Spitskop Mb.
1. Nord Witputz (Bowyer et al., 2022)
A3?
5. Hansburg (1) Wegkruip (2) Zuurburg (3) (Maloney et al., 2020)
3. Swartpunt (geochemical data from Bowyer et al., 2022; This study)
Uncertain lithostratigraphic correlation between sections 2 to 4. See text and fig. 5.
6. Arasab (Wood et al., 2015)
graduations = 50m in all sections
542.65±0.15 Ma
545.27±0.11 Ma
7. Grens (Wood et al., 2015)
! (>100km east of section 4)
6 (reworked?)
lower Nomtas Fm.
Huns
Feldschuhhorn
Spitsk.
Nomtas
Correlation (1)
Correlation (4)
4. Swartkloofberg (Grotzinger et al., 1995; Wood et al., 2015; Linnemann et al., 2019; This study)
Nomtas Fm.
Feld.
Huns Mb.
Nas.
Nudaus Fm.
Mo.
Zar.
Klipphoek
Mara
Kanies

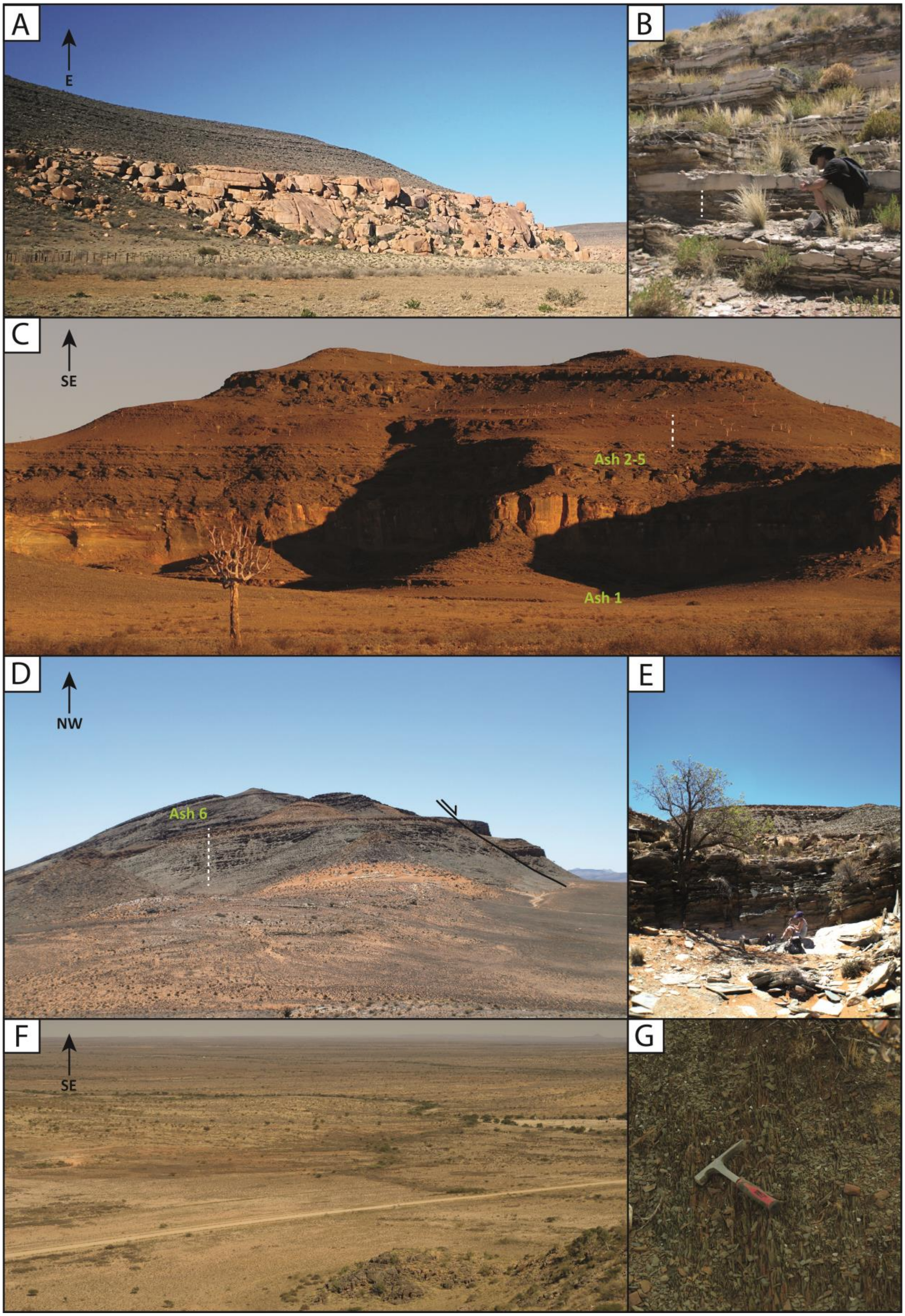

1158

1159 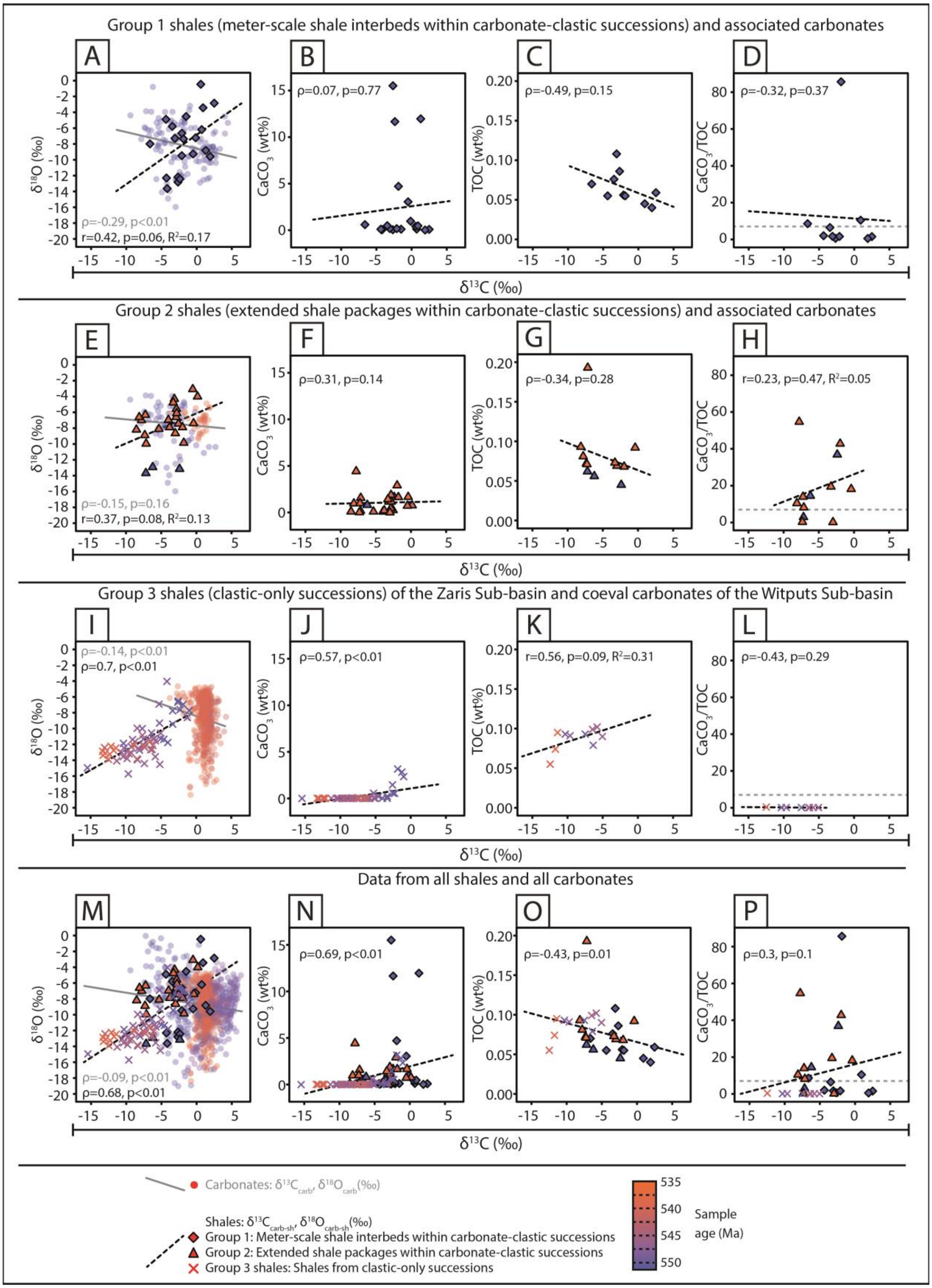
Group 1 shales (meter-scale shale interbeds within carbonate-clastic successions) and associated carbonates
A
ρ=-0.29, p<0.01
r=0.42, p=0.06, R²=0.17
B
ρ=0.07, p=0.77
C
ρ=-0.49, p=0.15
D
ρ=-0.32, p=0.37
Group 2 shales (extended shale packages within carbonate-clastic successions) and associated carbonates
E
ρ=-0.15, p=0.16
r=0.37, p=0.08, R²=0.13
F
ρ=0.31, p=0.14
G
ρ=-0.34, p=0.28
H
r=0.23, p=0.47, R²=0.05
Group 3 shales (clastic-only successions) of the Zaris Sub-basin and coeval carbonates of the Witputs Sub-basin
I
ρ=-0.14, p<0.01
ρ=0.7, p<0.01
J
ρ=0.57, p<0.01
K
r=0.56, p=0.09, R²=0.31
L
ρ=-0.43, p=0.29
Data from all shales and all carbonates
M
ρ=-0.09, p<0.01
ρ=0.68, p<0.01
N
ρ=0.69, p<0.01
O
ρ=-0.43, p=0.01
P
ρ=0.3, p=0.1
δ18O (‰)
CaCO3 (wt%)
TOC (wt%)
CaCO3/TOC
δ13C (‰)
Carbonates: δ13Ccarb, δ18Ocarb (‰)
Shales: δ13Ccarb-sh, δ18Ocarb-sh (‰)
Group 1: Meter-scale shale interbeds within carbonate-clastic successions
Group 2: Extended shale packages within carbonate-clastic successions
Group 3 shales: Shales from clastic-only successions
Sample age (Ma)
535
540
545
550

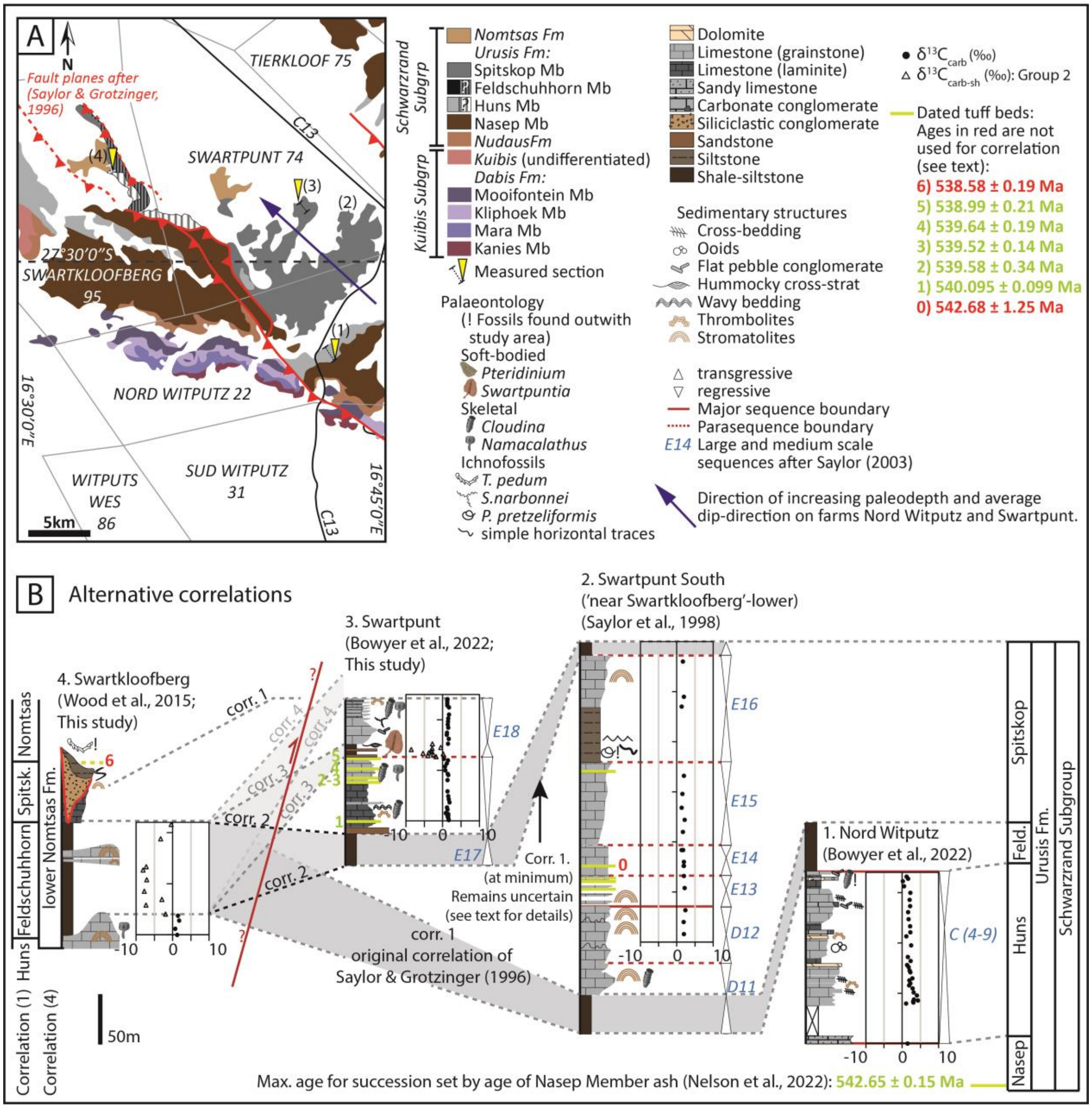
A
N
Fault planes after (Saylor & Grotzinger, 1996)
TIERKLOOF 75
SWARTPUNT 74
C13
27°30'0"S
SWARTKLOOFBERG 95
NORD WITPUTZ 22
SUD WITPUTZ 31
WITPUTS WES 86
16°30'0"E
16°45'0"E
5km
Schwarzrand Subgrp
Kuibis Subgrp
Nomtsas Fm
Urusis Fm:
Spitskop Mb
Feldschuhhorn Mb
Huns Mb
Nasep Mb
NudausFm
Kuibis (undifferentiated)
Dabis Fm:
Mooifontein Mb
Kliphoek Mb
Mara Mb
Kanies Mb
Measured section
Palaeontology (! Fossils found outwith study area)
Soft-bodied
Pteridinium
Swartpuntia
Skeletal
Cloudina
Namacalathus
Ichnofossils
T. pedum
S.narbonnei
P. pretzeliformis
simple horizontal traces
Dolomite
Limestone (grainstone)
Limestone (laminite)
Sandy limestone
Carbonate conglomerate
Siliciclastic conglomerate
Sandstone
Siltstone
Shale-siltstone
Sedimentary structures
Cross-bedding
Ooids
Flat pebble conglomerate
Hummocky cross-strat
Wavy bedding
Thrombolites
Stromatolites
transgressive
regressive
Major sequence boundary
Parasequence boundary
E14 Large and medium scale sequences after Saylor (2003)
Direction of increasing paleodepth and average dip-direction on farms Nord Witputz and Swartpunt.
δ13C carb (‰)
δ13C carb-sh (‰): Group 2
Dated tuff beds: Ages in red are not used for correlation (see text):
6) 538.58 ± 0.19 Ma
5) 538.99 ± 0.21 Ma
4) 539.64 ± 0.19 Ma
3) 539.52 ± 0.14 Ma
2) 539.58 ± 0.34 Ma
1) 540.095 ± 0.099 Ma
0) 542.68 ± 1.25 Ma
B Alternative correlations
4. Swartkloofberg (Wood et al., 2015; This study)
3. Swartpunt (Bowyer et al., 2022; This study)
2. Swartpunt South ('near Swartkloofberg'-lower) (Saylor et al., 1998)
1. Nord Witputz (Bowyer et al., 2022)
Nomtsas
Spitsk.
Feldschuhhorn
Huns
lower Nomtsas Fm.
Correlation (1)
Correlation (4)
corr. 1
corr. 2
corr. 3
corr. 4
Corr. 1. (at minimum) Remains uncertain (see text for details)
corr. 1 original correlation of Saylor & Grotzinger (1996)
E18
E17
E16
E15
E14
E13
D12
D11
C (4-9)
Spitskop
Feld.
Huns
Nasep
Urusis Fm.
Schwarzrand Subgroup
50m
-10 0 10
Max. age for succession set by age of Nasep Member ash (Nelson et al., 2022): 542.65 ± 0.15 Ma

1160

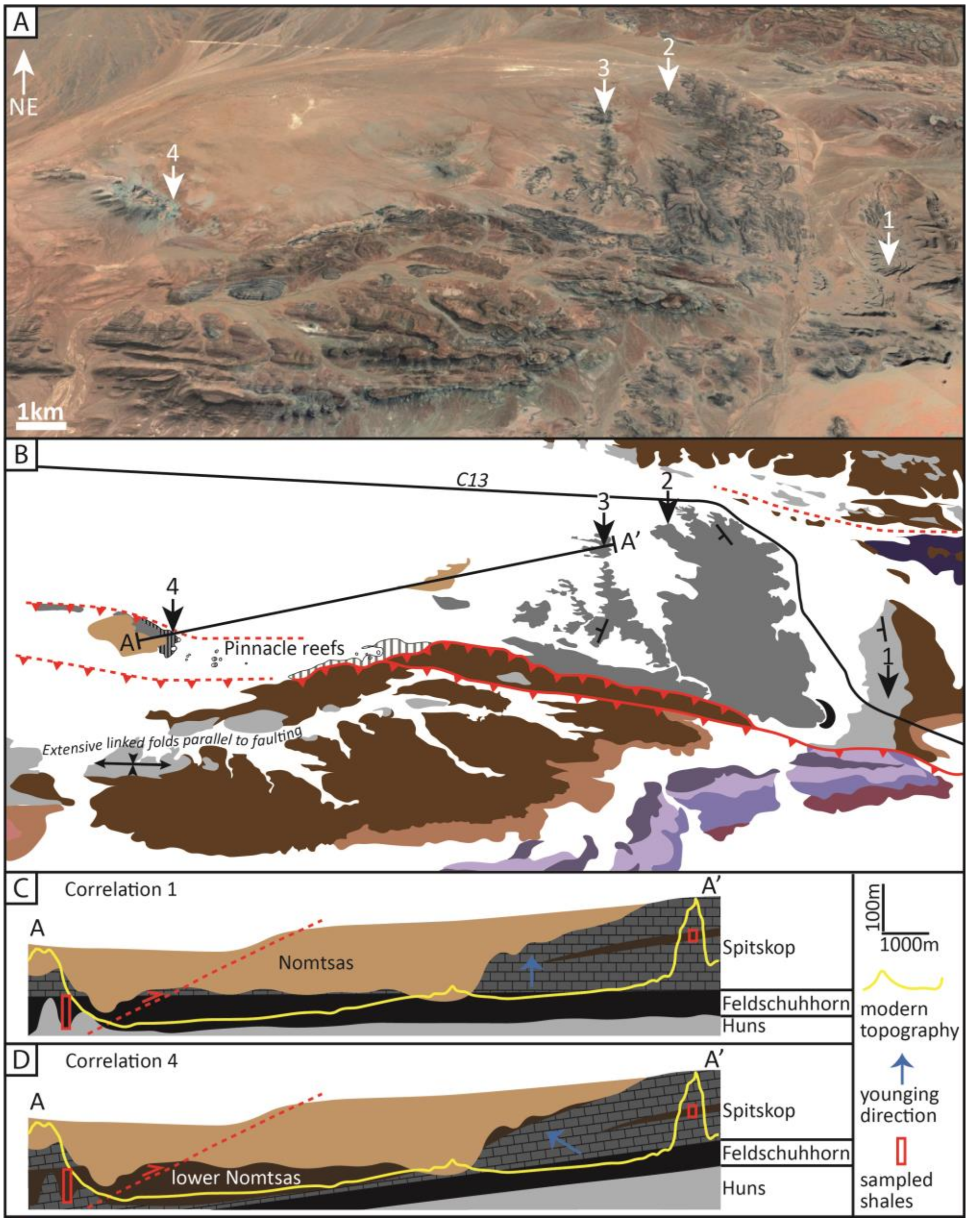

A
NE
1km
1
2
3
4
B
C13
A'
A
Pinnacle reefs
Extensive linked folds parallel to faulting
C
Correlation 1
A
A'
Nomtsas
Spitskop
Feldschuhhorn
Huns
100m
1000m
modern topography
younging direction
sampled shales
D
Correlation 4
lower Nomtsas

1161

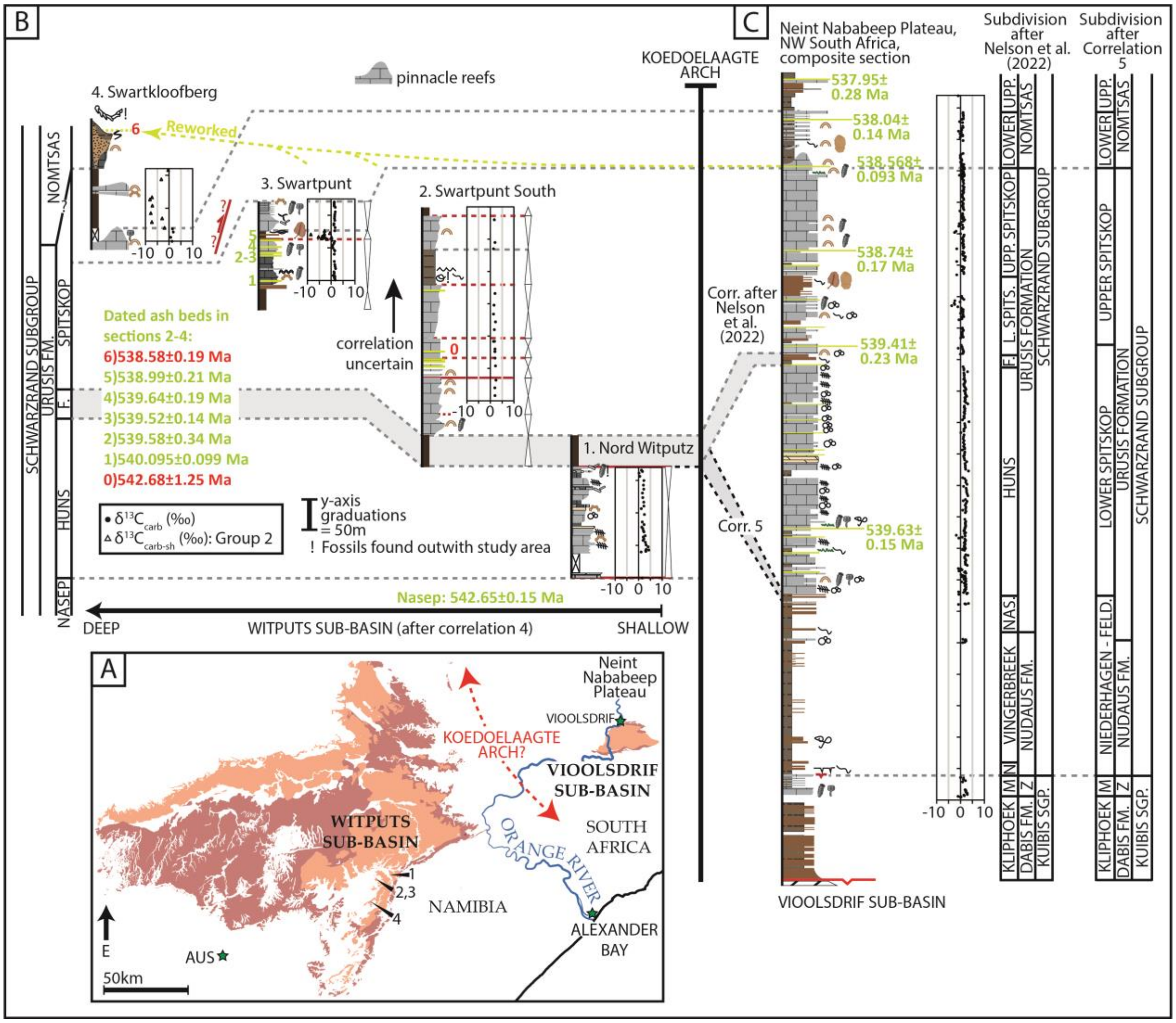
B
C
A
pinnacle reefs
KOEDOELAAGTE ARCH
4. Swartkloofberg
Reworked
3. Swartpunt
2. Swartpunt South
1. Nord Witputz
correlation uncertain
Dated ash beds in sections 2-4:
6)538.58±0.19 Ma
5)538.99±0.21 Ma
4)539.64±0.19 Ma
3)539.52±0.14 Ma
2)539.58±0.34 Ma
1)540.095±0.099 Ma
0)542.68±1.25 Ma
y-axis graduations = 50m
! Fossils found outwith study area
Nasep: 542.65±0.15 Ma
DEEP
WITPUTS SUB-BASIN (after correlation 4)
SHALLOW
SCHWARZRAND SUBGROUP
URUSIS FM.
NOMTSAS
SPITSKOP
HUNS
NASEP
Neint Nababeep Plateau, NW South Africa, composite section
537.95± 0.28 Ma
538.04± 0.14 Ma
538.568± 0.093 Ma
538.74± 0.17 Ma
539.41± 0.23 Ma
539.63± 0.15 Ma
Corr. after Nelson et al. (2022)
Corr. 5
VIOOLSDRIF SUB-BASIN
Subdivision after Nelson et al. (2022)
Subdivision after Correlation 5
LOWER SPITSKOP
UPPER SPITSKOP
NIEDERHAGEN - FELD.
VINGERBREEK
NUDAUS FM.
KLIPHOEK
DABIS FM.
KUIBIS SGP.
URUSIS FORMATION
SCHWARZRAND SUBGROUP
Neint Nababeep Plateau
VIOOLSDRIF
KOEDOELAAGTE ARCH?
VIOOLSDRIF SUB-BASIN
WITPUTS SUB-BASIN
ORANGE RIVER
SOUTH AFRICA
NAMIBIA
ALEXANDER BAY
AUS
50km

1163 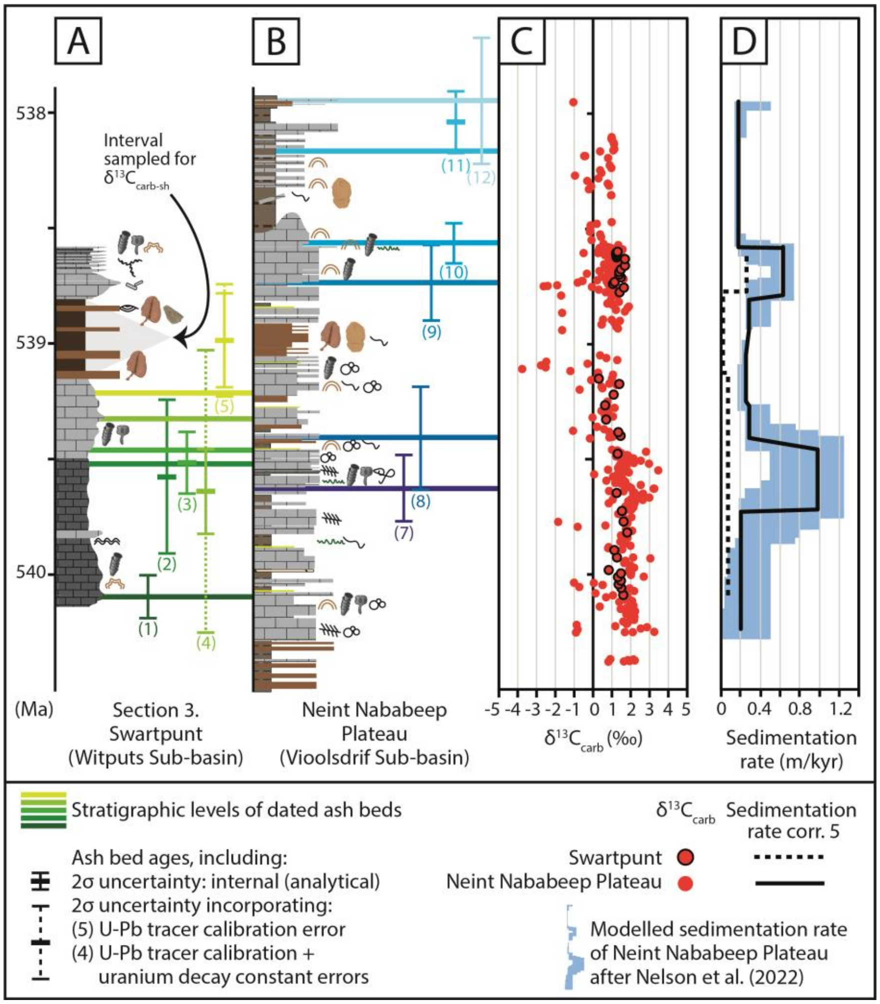
A
B
C
D
538
539
540
(Ma)
Interval sampled for δ13Ccarb-sh
(1)
(2)
(3)
(4)
(5)
(7)
(8)
(9)
(10)
(11)
(12)
Section 3. Swartpunt (Witputs Sub-basin)
Neint Nababeep Plateau (Vioolsdrif Sub-basin)
-5 -4 -3 -2 -1 0 1 2 3 4 5
δ13Ccarb (‰)
0 0.4 0.8 1.2
Sedimentation rate (m/kyr)
Stratigraphic levels of dated ash beds
Ash bed ages, including:
2σ uncertainty: internal (analytical)
2σ uncertainty incorporating:
(5) U-Pb tracer calibration error
(4) U-Pb tracer calibration + uranium decay constant errors
δ13Ccarb
Sedimentation rate corr. 5
Swartpunt
Neint Nababeep Plateau
Modelled sedimentation rate of Neint Nababeep Plateau after Nelson et al. (2022)

1164 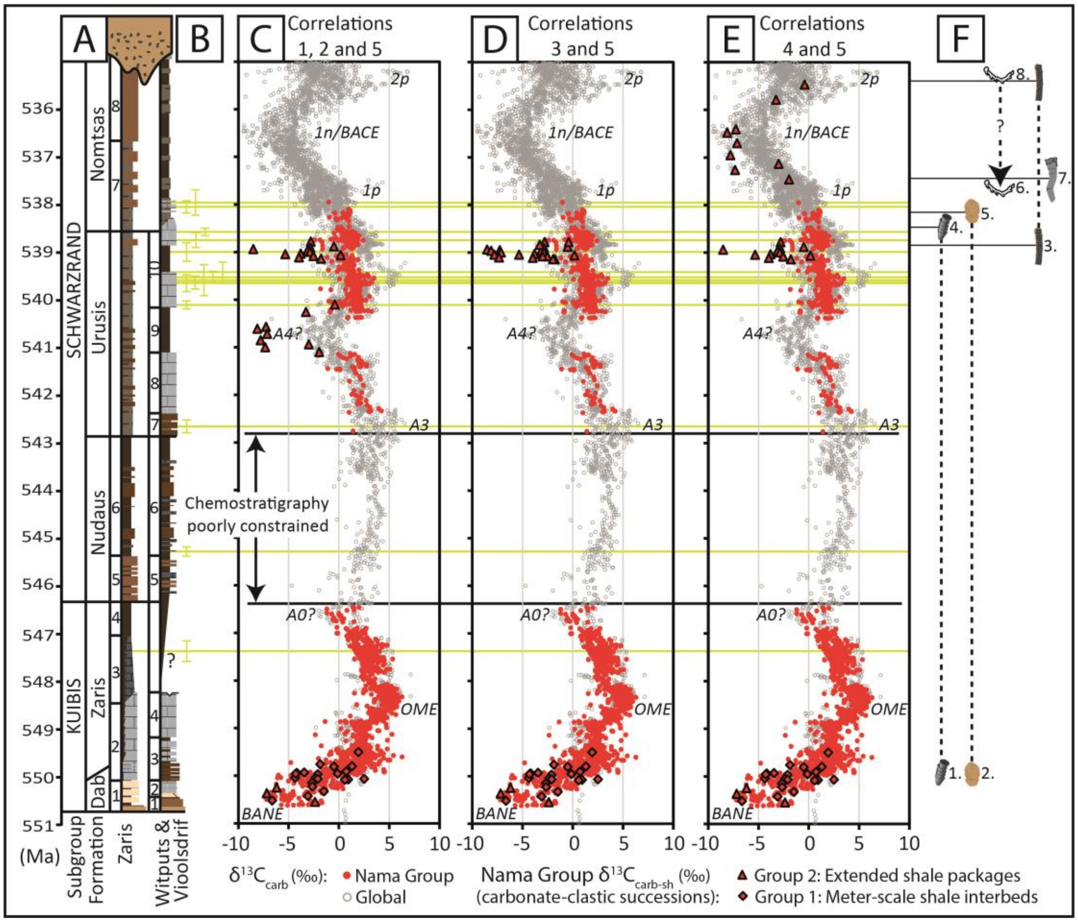
A
B
C
Correlations 1, 2 and 5
D
Correlations 3 and 5
E
Correlations 4 and 5
F
SCHWARZRAND
KUIBIS
Nomtsas
Urusis
Nudaus
Zaris
Dab
Chemostratigraphy poorly constrained
2p
1n/BACE
1p
A4?
A3
A0?
OME
BANE
Subgroup
Formation
Zaris
Witputs & Vioolsdrif
(Ma)
δ13Ccarb (‰): Nama Group
Global
Nama Group δ13Ccarb-sh (‰) (carbonate-clastic successions):
Group 2: Extended shale packages
Group 1: Meter-scale shale interbeds